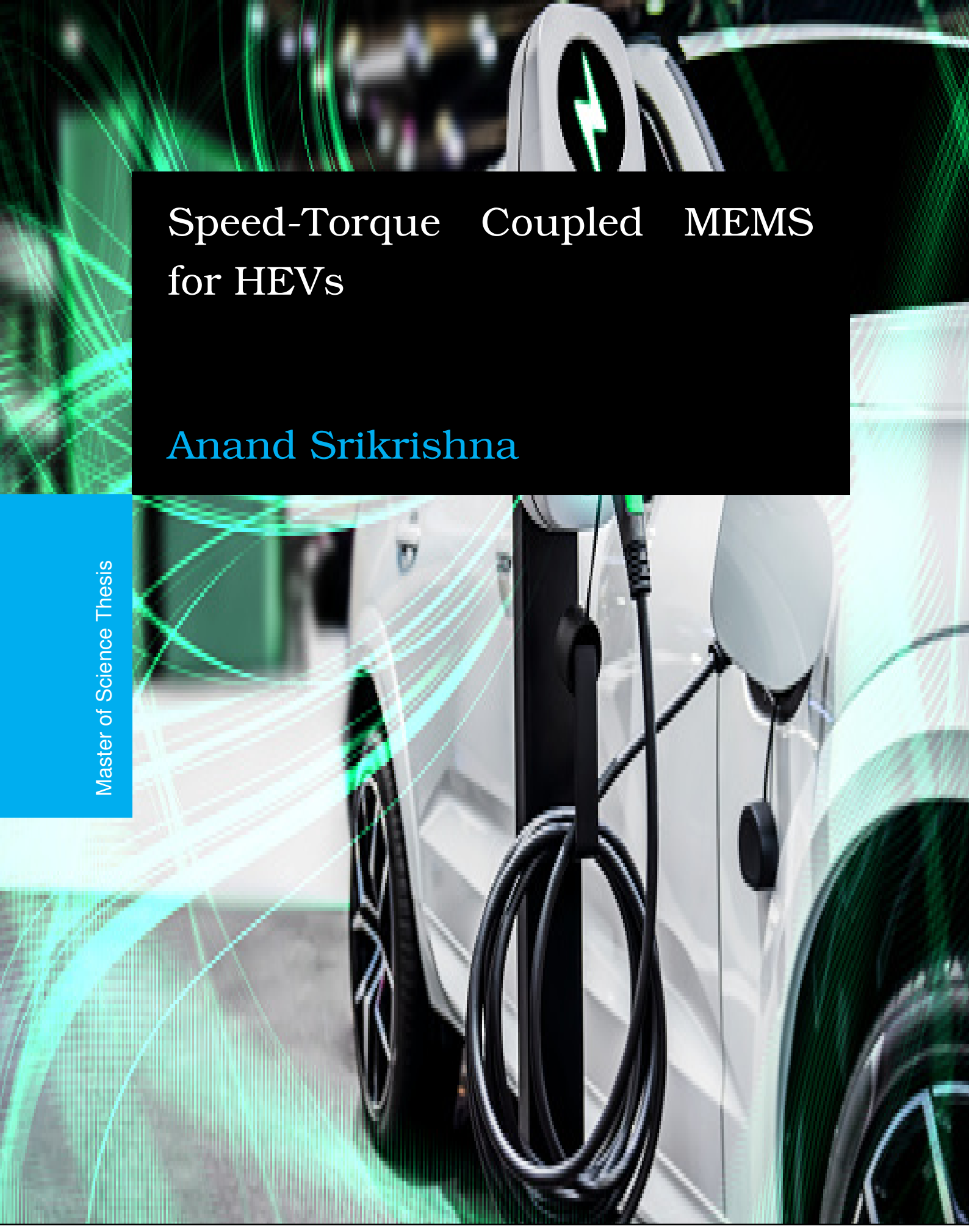

Speed-Torque Coupled MEMS for HEVs

Anand Srikrishna

Master of Science Thesis

TU Delft Delft University of Technology

Delft Center for Systems and Control

Speed-Torque Coupled MEMS for HEVs

MASTER OF SCIENCE THESIS

For the degree of Master of Science in Systems and Control at Delft University of Technology

Anand Srikrishna

August 24, 2023

Faculty of Mechanical, Maritime and Materials Engineering (3mE) · Delft University of Technology

TNO supported the work in this Master thesis. Their cooperation is hereby gratefully acknowledged.

Abstract

Fuel consumption reduction in Hybrid Electric Vehicles (HEV) powertrains has been an important area of research over the past few decades. HEV powertrains have two energy sources : fuel and battery. The important task of splitting the energy/power demand between both these sources is performed by the Energy Management Systems (EMS). There are many EMS methods and the focus of this thesis is on a method called Modular ECMS (MEMS) implemented by TNO as per [13]. MEMS finds the optimal power split among the subsystems by minimizing the energy loss in each subsystem. This strategy assumes that the operating speed of the subsystems of the powertrains is known and uses this knowledge to find the optimal power split and torque among these subsystems.

The objective of this thesis is to find the optimal operating speed of the subsystems as well. This is done by a least squares fitting of the objective function and constraints as functions of subsystems speed and torque. A revised Optimal Control Problem (OCP) is formulated as a quadratic programming problem of speed and torque and is termed as Speed-Torque Coupled MEMS (ST-MEMS). The ST-MEMS algorithm is tested on a series-hybrid wheel loader powertrain model and its performance is compared to MEMS, with the model and data provided by TNO. It is concluded that the ST-MEMS, while adding the speed and torque bounds as degrees of freedom, does not achieve a good distribution of power between the 2 sources. The reason for this behaviour is analyzed and an alternate approach is suggested for future work.

Contents

List of Figures

List of Tables

Acknowledgments

"Life is like Bellman Principle. The future is not determined by the past, it purely depends on what we do in the present. Let's make best use of the present."

I would like to sincerely thank my supervisors Peyman Mohajerin Esfahani from TU Delft and Steven Wilkins from TNO for their guidance during the period of this thesis. Their constant appreciation and push towards improvement has provided me with an enriching experience. I would also sincerely thank my Ph.D. Supervisor, Reza Rahimi Baghbadorani for his invaluable inputs, especially whenever there was a roadblock ahead.

I cannot express enough gratitude to my support system : my parents Srikrishnan and Saroja, my sister Meera and brother-in-law Karthik. Apart from them, all my friends who have helped me enjoy the present, challenge and motivate me at the same time and spreading positivity all over my life.

Finally, I would like to thank Guru and God for all the moments.

Delft, University of Technology
August 24, 2023

Anand Srikrishna

Chapter 1

Introduction

Powertrain modelling and control has been an important area of research for many automotive manufacturers. The aim has always been to lower their fuel consumption and reduce emissions. An important powertrain application, especially over the past decade, are Hybrid Electric Vehicles (HEV). Many governments encourage the use of HEVs as they improve local air quality and reduce fuel costs. The sales of HEVs in the Netherlands as a percentage of passenger car sales has increased from 4.7% to 11.8% from 2016 to 2022. The number of charging points in Netherlands has almost tripled over the last 5 years. [1]

Fuel consumption reduction in HEVs has been an important area of research over the past decade. HEVs have electric actuators and storage systems such as batteries which provide additional bidirectional degrees of freedom for an energy source, apart from the fuel or the Internal Combustion Engine (ICE). Thus an important task is splitting the energy/power demand between both these sources in the most optimal manner possible, so as to reduce the fuel consumption and overall energy consumption costs. This is the role of Energy Management Systems (EMS). [15] A method to achieve EMS is based on optimization. Optimization-based (OB) EMS minimize a cost function, like fuel consumption or total energy cost combined with emission levels or battery life [15], depending on certain constraints, thus solving an Optimal Control Problem (OCP). A popular OB method for energy management is Equivalent Consumption Minimization Strategy (ECMS) which shall be discussed in more detail as it is the method of interest in [13] and currently implemented in TNO, thus being the centre of focus of the thesis.

1-1 ECMS

ECMS is a control strategy for HEV which was introduced by Paganelli in [9]. The aim was to represent the global optimal problem (usually solved when driving cycles are known a-priori) to an instantaneous energy flow problem. ECMS is formed on the notion that the energy storage device (battery) can also be seen as a fuel tank, from which if energy is consumed, it has to be provided again by using fuel or by regenerative braking (recharging of the battery when vehicle is decelerating). [8]

There are two scenarios which need to be discussed :

- Discharge case : Battery power is positive and is being used. In this case fuel is be used to drive the vehicle and recharge the battery, which means there will be fuel consumption.
- Charge case : Battery power is negative and is used instead of fuel to drive the vehicle and which means there will be fuel savings.

The equivalence between the energy consumption from battery and fuel is established by multiplying the battery power with an equivalent factor (EF) to represent the cost of consuming the battery power as a multiple of the cost of consuming the fuel power.

Thus, the overall fuel consumption becomes,

$$\dot{m}_{f,eqv}(i) = \dot{m}_f(i) + \dot{m}_{batt}(i) \tag{1-1}$$

where $\dot{m}_{f,eqv}$ is the equivalent fuel flow rate, $\dot{m}_f$ is the flow rate from the fuel consumption and $\dot{m}_{batt}$ is the flow rate from battery power consumption and i is the time instant. [8]

A simplified relationship between flow rate $(\dot{m})$ and power produced (P) in the fuel and battery is given in [8] as :

$$\dot{m}_f(i) \propto P_f(i) \tag{1-2}$$

$$\dot{m}_{batt}(i) = s(i)P_{batt}(i) \tag{1-3}$$

where $s(i)$ is the EF. Thus, the equivalent power P_{eqv} is defined as,

$$P_{eqv}(i) = P_f(i) + s(i)P_{batt}(i) \tag{1-4}$$

where i is the time instant.

The EF changes with time depending on the efficiency of conversion of fuel energy to electrical or

vice-versa. Depending on P_{batt}, the equivalent fuel consumption P_{eqv} can be either positive or negative which represent fuel consumption or savings.

1-1-1 Modular ECMS (MEMS)

MEMS is an idea discussed in [13] and is currently implemented in TNO. This idea is based on 2 concepts.

The first of them is the concept of distributed control [14]. The MEMS approach in [13] uses distributed control by dividing the HEV into subsystems such as Internal Combustion Engine (ICE), High-Voltage Battery (HVB), Brakes (BRA), Electric Machine (EM) etc. and optimizing for fuel consumption in each of these subsystems. The approach also imposes a constraint which establishes subsystem communication by using a power flow diagram. Nodes are introduced in the system where inflow and outflow of power to or from the subsystems to each of these nodes are used for these constraints.

The next concept is that minimizing the fuel consumption by the ICE is equivalent to minimizing the cumulative energy losses in each subsystem as established by [12]. This is done by choosing an appropriate cost coefficient for input and output power.

Before discussing the Optimal Control Problem (OCP), the below mathematical notations are defined.

- $m \in \mathscr{M} = \{1, ...M\}$ indicates the subsystem index where M is the number of subsystems. They are also represented without indexing and in terms of the subsystem name like ICE,HVB etc.
- $k \in \mathscr{K} = \{0, 1, ...K-1\}$ indicates the time horizon instance where K is the horizon length
- $u_{m,k}$ is the input power of subsystem m at time k
- $y_{m,k}$ is the output power of subsystem m at time k
- $x_{m,k}$ is the energy of the subsystems which have a storage capacity. e.g. $x_{m,k}$ can be the SOC of the battery at time k.
- $v_{n,k}$ is the exogenous load signal at node n at time instant k where $n \in \mathscr{N} = \{1, ...N\}$ indicates the node index and N is the number of nodes

Thus, the objective function is defined as the cumulative energy loss,

$$\min_{u_{m,k}, y_{m,k}} \sum_{m \in \mathscr{M}} \sum_{k \in \mathscr{K}} c_m u_{m,k} - d_m y_{m,k} + \lambda_k u_{hvb,k} \tag{1-5}$$

where c_m and d_m are energy loss cost coefficients for each subsystem and λ_k is the EF at time instant k.

The first constraint is quadratic and is defined for the input-output power relation,

$$y_{m,k} + \frac{1}{2} q_{m,k} u_{m,k}^2 + f_{m,k} u_{m,k} + e_{m,k} = 0 \tag{1-6}$$

$\forall\, m \in \mathscr{M}, k \in \mathscr{K}$

The coefficients $q_{m,k}$, $f_{m,k}$ and $e_{m,k}$ are time-varying, efficiency coefficients. These coefficients are dependent on the flow variable of each subsystem. For subsytems which involve mechanical energy (ICE and EM), the coefficients are dependent on their operating speed and for HVB, the coefficients are dependent on SOC. Thus, for speed-dependent coefficients, these coefficients are represented by :

$$q_{m,k} = q_{m,k}(\omega_{m,k}), f_{m,k} = f_{m,k}(\omega_{m,k}), e_{m,k} = e_{m,k}(\omega_{m,k}) \tag{1-7}$$

$\forall\, m \in \mathscr{M}$ corresponding to ICE, EM, $k \in \mathscr{K}$

The input power is bounded using a linear inequality constraint,

$$\underline{u}_{m,k} \leq u_{m,k} \leq \bar{u}_{m,k} \tag{1-8}$$

$\forall\, m \in \mathscr{M}, k \in \mathscr{K}$

Finally, the interconnection between subsystems based on the power flow between nodes to establish distributed control,

$$\sum_{m \in \mathscr{M}} \Gamma_m u_{m,k} + \Theta_m y_{m,k} + \frac{1}{M} v_k = 0 \tag{1-9}$$

$\forall\, m \in \mathscr{M}, k \in \mathscr{K}$ where $\Gamma \in \mathbb{R}^N$ and $\Theta \in \mathbb{R}^N$ are inter-connectivity vectors in which n^{th} element being -1 if power flow to node n is positive, 0 if there is no power flow to node n and 1 if the power flow to node n is negative. The positive and negative power flow can be decided depending on whether the power flows into or out of the node. This constraint is explained in detail in chapter 2.

Additionally, there are constraints specific to energy storage subsystems, i.e., HVB which describe its SOC evolution and bounds.

Thus, the Optimal Control Problem (OCP) is formulated with Equation 1-5 as the objective function with Equation 1-6 to Equation 1-9 as the constraints. To achieve distributed control, dual decomposition is performed in the OCP. The objective function in Equation (1-5) is modified into a partial Lagrangian to include a Lagrangian multiplier $\mu_k \in \mathbb{R}^N$ and the interconnectivity constraint in Equation (1-9). The new objective function is :

$$L(\{u_{m,k}, y_{m,k}, \mu_k\}) = \sum_{m \in \mathscr{M}} \sum_{k \in \mathscr{K}} c_m u_{m,k} - d_m y_{m,k} + \mu_k^T (\Gamma_m u_{m,k} + \Theta_m y_{m,k} + \frac{1}{M} v_k) + \lambda_k u_{hvb,k} \quad (1\text{-}10)$$

The partial Lagrangian dual function of the OCP is then given by,

$$g(\{\mu_k\}) = \min_{\{u_{m,k}, y_{m,k}\}} L(\{u_{m,k}, y_{m,k}, \mu_k\}) \quad (1\text{-}11)$$

$$= \mu_k^T v_k + g_m(\{\mu_k\}) \quad (1\text{-}12)$$

$\forall m \in \mathscr{M}$ where,

$$g_m(\{\mu_k\}) = \min_{\{u_{m,k}, y_{m,k}\}} \sum_{k \in \mathscr{K}} (c_m + \mu_k^T \Gamma_m) u_{m,k} - (d_m - \mu_k^T \Theta_m) y_{m,k} \quad (1\text{-}13)$$

$\forall m \in \mathscr{M} \backslash \{\text{HVB}\}$ subject to constraints in Equation (1-6) to Equation (1-8)

and for $m = \{\text{HVB}\}$,

$$g_{hvb}(\{\mu_k\}) = \min_{\{u_{hvb,k}, y_{hvb,k}\}} \sum_{k \in \mathscr{K}} (c_{hvb} + \mu_k^T \Gamma_{hvb}) u_{hvb,k} - (d_{hvb} - \mu_k^T \Theta_{hvb}) y_{hvb,k} + \lambda_k u_{hvb,k} \quad (1\text{-}14)$$

subject to constraints in Equation (1-6) to Equation (1-8) and additional State-of-Charge (SOC) constraints given as :

$$\begin{aligned} x_{hvb,k+1} &= A_{hvb} x_{hvb,k} + B_{hvb,w} w_{hvb,k} + B_{hvb,u} u_{hvb,k} \\ \underline{x}_{hvb,k} &\leq x_{m,k} \leq \bar{x}_{hvb,k} \end{aligned} \quad (1\text{-}15)$$

where $w_{hvb,k}$ is a known load signal at time instant k and $\underline{x}_{hvb,k}$ and $\bar{x}_{hvb,k}$ are the upper and lower bounds for the SOC.

The above problem is called the primal problem. To complete the distributed optimization, the dual problem below is solved :

$$\max_{\{\mu_k\}} g(\{\mu_k\}) = d^* \quad (1\text{-}16)$$

$\forall k \in \mathscr{K}$ which is the dual optimal value of Equation (1-5).

Thus, the overall OCP can be written as a min-max problem as :

$$\begin{aligned}
&\min_{u_m, y_m} \sum_{m\in\mathscr{M}} \sum_{k\in\mathscr{K}} (c_m u_{m,k} - d_m y_{m,k} + \mu_k^T(\Gamma_m u_{m,k} + \Theta_m y_{m,k} + \frac{1}{M} v_k)) + \lambda_k u_{hvb,k} \\
&\text{s.t. } y_{m,k} + \frac{1}{2} q_{m,k} u_{m,k}^2 + f_{m,k} u_{m,k} + e_{m,k} = 0 \\
&\quad \underline{u}_{m,k} \leq u_{m,k} \leq \bar{u}_{m,k} \\
&\quad x_{hvb,k+1} = A_{hvb} x_{hvb,k} + B_{hvb,w} w_{hvb,k} + B_{hvb,u} u_{hvb,k} \\
&\quad \underline{x}_{hvb,k} \leq x_{hvb,k} \leq \bar{x}_{hvb,k}
\end{aligned} \tag{1-17}$$

$\forall\, m \in \mathscr{M}, k \in \mathscr{K}$

To then obtain d^* as per Equation (1-16), the maximization of the Lagrangian multiple is done using a steepest ascent at each iteration s.

$$\mu_k^{s+1} = \mu_k^s + \alpha_k^s \sum_{m\in\mathscr{M}} (\Gamma_m u_{m,k}^s + \Theta_m y_{m,k}^s + \frac{1}{M} v_k) \tag{1-18}$$

$\forall k \in \mathscr{K}$ where α_k is the step size of the ascent and s is the iteration number. The choice of this step size is elaborated in [12], where it is based on satisfying the primal feasibility condition in Equation (1-9) combined with an adaptation based on a Newton scheme.

Torque Split

The speed of the subsystems are known and the optimal power is found by solving the OCP. The power for subsystems m which involve mechanical energy like ICE and EM are defined using [13] as :

$$P_m = T_m \omega_m \tag{1-19}$$

where P_m can be input power u_m or output power y_m depending on whether mechanical power flows in or out of the subsystem respectively. T_m is the torque of the subsystem. Thus, with known speed and power, the torque split for each subsystem is found after solving the optimization problem thus ensuring the optimal operating torque for the particular speed.

Gear Selection

The optimal gear selection logic is a straightforward rule-based approach. Depending on the current speed, optimal power obtained on solving the OCP, the cost of operating at each gear is calculated. The gear with the minimal cost of operating is thus obtained. Then, depending on a preset cost of changing gears, a decision is made whether to change the gear or continue with the current gear. All these decisions are made using look-up tables.

The advantages of this algorithm to be preserved in this thesis are :

- The method has flexibility and modularity. In case, another subsystem needs to be added in the system, e.g. a motor or generator, it needs to be added in the power flow diagram, connected to the correct nodes and accounted for in the interconnection matrices in Equation (1-9). The rest of the distributed optimization algorithm can be carried out as it is. Thus, this approach can be adapted to various powertrain architectures.
- Due to modularity, the computational speed is high. This is the main result of the paper as it states that the optimal fuel consumption reduction can be achieved in 45 iterations of the dual decomposition problem and can be safely reduced to 40 iterations.
- Due to a convex formulation of the OCP, there is a guarantee of optimality.

A particular room of improvement of interest in this thesis is:

- In a series-hybrid topology, the vehicle and the engine can run at different speeds as the engine is detached from the wheels. The generator and motor can also operate at different speeds. In the current set up, these speeds are not optimized, only the torques are optimized. The speed of these subsystems are taken as an input to the optimization problem and are used for the speed-dependent constraints. By optimizing the power-split with respect to speed as well, the engine, generator, motor etc. can run at more optimal operating points.

In conclusion, the gap about speed-torque coupled MEMS will be the main focus for the rest of the and thesis. Additionally, the modularity and computational speed is to be preserved.

Chapter 2

Series-Hybrid Wheel Loader

This chapter deals with the system on which the MEMS algorithm is implemented. The system of concern is a series-hybrid wheel loader. A wheel loader is heavy machinery typically used in construction. In wheel loaders, an engine is typically used to move a hydraulic pump and also an energy converter like a generator. The hydraulic pump is then used to operate an arm to lift and transport material such as dirt, gravel, sand, debris etc. [7]. A typical wheel loader is shown in Figure 2-1. [2]

Figure 2-1: Wheel Loader (Source : [2])

The important pre-requisite information and assumptions considered are given as follows :

- The longitudinal model is considered for the vehicle, thus modelling the left and right part of the wheel as a single model. Therefore, yaw moment is not considered.
- The power losses in the gearbox are negligible.

- The gearshift strategy is fixed, resulting in the knowledge of the rotational speed of the drive line $\omega_{m,k}$ for every subsystem $m \in \mathscr{M}$ and at every time instant $k \in \mathscr{K}$.
- This configuration includes four external load signals, denoted as $v_k = [v_{1,k}\ v_{2,k}\ v_{3,k}\ v_{4,k}]^T \in \mathbb{R}^4$. These signals represent the drive power needed to operate a specific drive cycle, the power consumption of high-voltage auxiliary systems, and the power consumption of low-voltage auxiliary systems. It is assumed that these signals are known for each time instant $k \in \mathscr{K}$.

2-1 Powertrain Topology

The powertrain is the set of components which is responsible for the conversion of energy from the source of power to the motion of driving components(wheels). The powertrain usually contains an energy source like a High-Voltage Battery (HVB), energy convertors or Electric Machine (EM) like motors/generators, gear mechanisms and an Internal Combustion Engine (ICE). Depending on the powertrain topology, HEV can be broadly classified as [17]:

- **Series-hybrid** : A series-hybrid powertrain has at least 2 EMs and the ICE is not directly used to drive the wheel. The engine converts potential energy to mechanical energy, provides it to the generator which runs a motor via an inverter as shown in Figure 2-2a. The motor can also receive the power from the battery via an inverter. This motor is used to drive the transmission.
- **Parallel-hybrid** : A parallel-hybrid powertrain has one EM and the ICE is directly used to drive the wheel. The main difference is the presence of a mechanical coupler which combines the torque from the motor and the engine, as shown in Figure 2-2b. The motor is powered by the battery via an inverter.

This is relevant for the gap discussed about running the subsystems at different speeds as it is not possible to do so in a parallel-hybrid powertrain topology. This is because the ICE is directly connected to the wheels and thus its speed has to be determined by the wheel rotation speed itself. In a series-hybrid topology, since the engine and the wheels are not connected directly, they can run at different speeds and hence, optimization of the engine speed is possible.

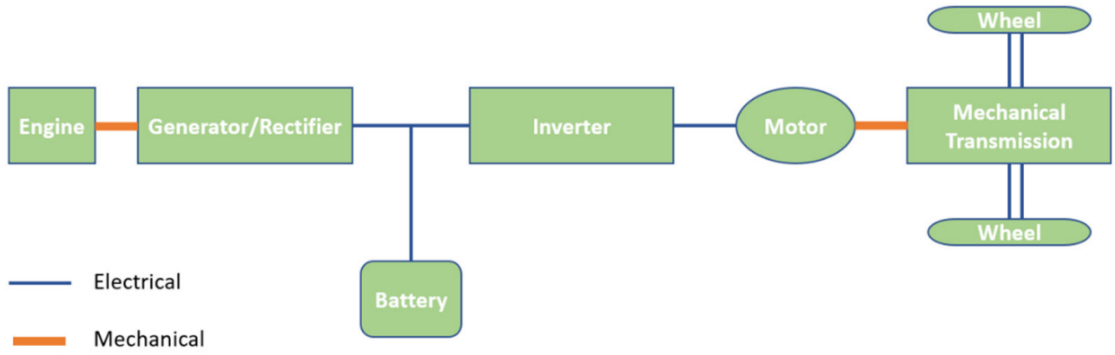

(a) Schematic of a series-hybrid powertrain [17]

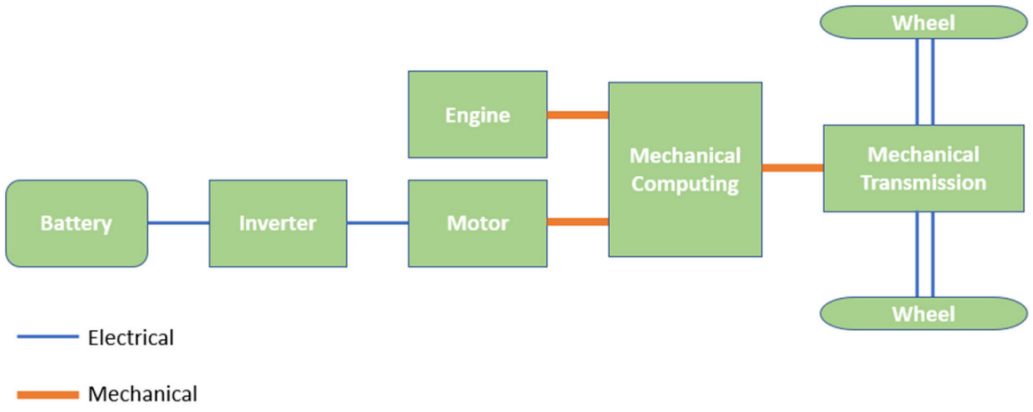

(b) Schematic of a parallel-hybrid powertrain [17]

Figure 2-2: Types of Powertrain Topology

The system of interest is a series-hybrid system as shown in Figure 2-3. In this figure, the blue lines indicate the flow of mechanical energy and green lines indicate the flow of electrical energy. Thus it consists of two Electric Machine (EM)s or Motor/Generator (MG), one acting as a generator to receive mechanical energy from the ICE and the other acting as a traction motor to provide mechanical energy to drive the transmission/wheels. Going upstream from the transmission, the wheels are connected to a gearbox which houses its own control unit. The gearbox receives mechanical energy from the traction motor also known as MG2. MG2 can receive electrical energy from 2 sources :

1. A 350V HVB with a DC-to-DC Converter, thus providing an output voltage of 700V.
2. A generator also known as MG1. MG1 receives mechanical energy from the ICE through a gearset with a fixed gear ratio.

The electrical energy from MG1 can also be used to charge the battery. The ICE additionally moves a hydraulic pump used to lift and move materials simultaneous to providing mechanical energy to the

generator. Both the MGs contain their own inverters to convert DC from/to the battery to AC. Additionally, the HVB along with the DC-to-DC converter is connected to a Electric Brake Resistor (EBR). The EBR is required when the HVB cannot get charged or when the generator cannot get propelled by the ICE. The EBR carries out the important function of regenerative braking, which is a conversion of the mechanical energy of the braking process to other forms of energy such that it acts along with the friction brake system to produce the required braking energy. Regenerative braking can either be carried out by the reverse torque used by the motor for braking which is converted to regenerative current and charges the battery or it can be converted to heat by the EBR. [5] eAUX/eBooster is used for engine transients set at zero. It can be considered as a starter motor, which enables the engine to start its operation under its own power until it reaches at an operation point where combustion can take over. [6]

The green connections next to the ICE in Figure 2-3 is the low voltage connections accompanying the ICE and are not considered in the model for optimization as they are used only to start the engine and have no role later in terms of controlling the engine speed/torque.

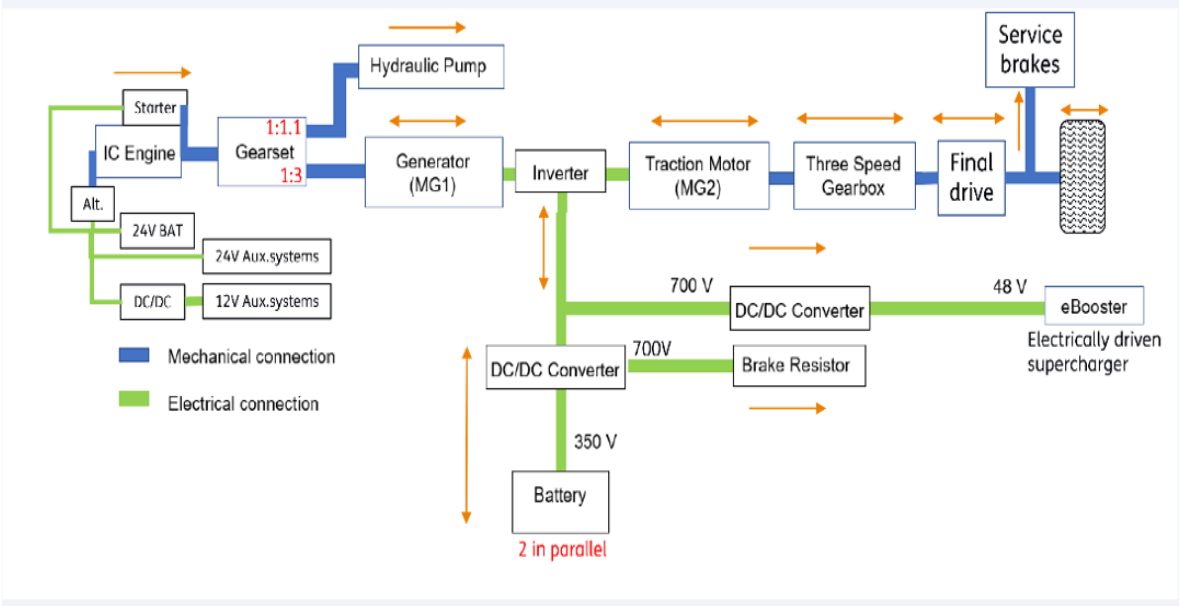

Figure 2-3: Wheel Loader Powertrain Topology (Source : TNO)

Using the topology in Figure 2-3, the set of subsystems $\mathscr{M}$ is formulated as :

$$\mathscr{M} := \{\text{ICE}, \text{MG1}, \text{MG2}, \text{GB3}, \text{EBR}, \text{BRA}, \text{HVB}\} \tag{2-1}$$

Although integers are used to define the set, the subsystems can be indexed and represented as an integer. For the rest of this report, this indexing is neglected and the definition in Equation 2-1 is followed.

Next, using this topology, the inter-connectivity matrices in Equation 1-9 also can be defined. For this, the power flow diagram given in Figure 2-4 has to be examined.

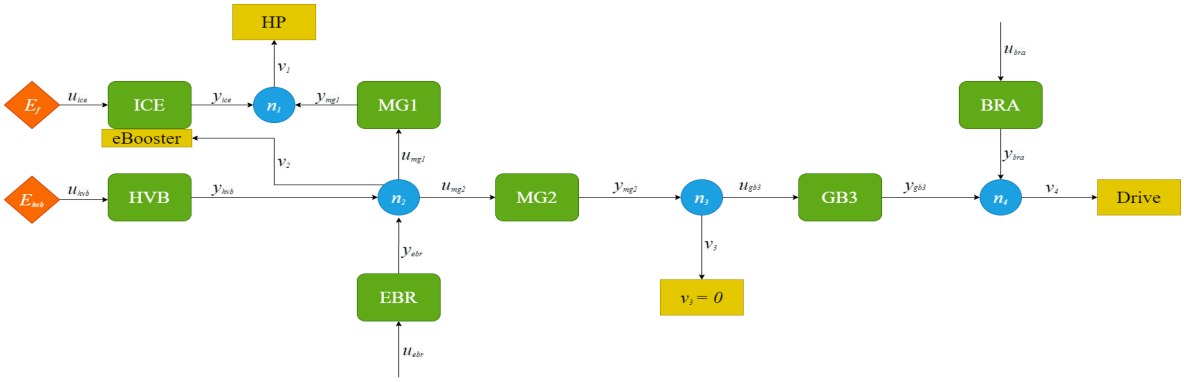

Figure 2-4: Power Flow Diagram (Source : TNO)

The subsystems are represented using the green boxes and the power flow is divided into 4 nodes. The auxiliary parts such as eAUX, HP and transmission are represented using yellow boxes. The input, output and external powers are examined at the nodes with the convention that the power into the node is negative and power out of the node is positive (as shown in the figure).

The power flow equation for each node can be written as :

$$\begin{aligned}
&\textbf{Node 1 :}\ v_1 - y_{ice} - y_{mg1} = 0 \\
&\textbf{Node 2 :}\ v_2 - y_{hvb} - y_{ebr} + u_{mg1} + u_{mg2} = 0 \\
&\textbf{Node 3 :}\ v_3 - y_{mg2} + u_{gb3} = 0 \\
&\textbf{Node 4 :}\ v_4 - y_{bra} - y_{gb3} = 0
\end{aligned} \tag{2-2}$$

The constraint in Equation 1-9 are derived from these node balance equations and the matrices Γ and Θ for each subsystem as are formulated as :

$$\begin{aligned}
\Gamma_{ice} &= \begin{bmatrix} 0 & 0 & 0 & 0 \end{bmatrix}^T, & \Theta_{ice} &= \begin{bmatrix} -1 & 0 & 0 & 0 \end{bmatrix}^T \\
\Gamma_{mg1} &= \begin{bmatrix} 0 & 1 & 0 & 0 \end{bmatrix}^T, & \Theta_{mg1} &= \begin{bmatrix} -1 & 0 & 0 & 0 \end{bmatrix}^T \\
\Gamma_{mg2} &= \begin{bmatrix} 0 & 1 & 0 & 0 \end{bmatrix}^T, & \Theta_{mg2} &= \begin{bmatrix} 0 & 0 & -1 & 0 \end{bmatrix}^T \\
\Gamma_{gb3} &= \begin{bmatrix} 0 & 0 & 1 & 0 \end{bmatrix}^T, & \Theta_{gb3} &= \begin{bmatrix} 0 & 0 & 0 & -1 \end{bmatrix}^T \\
\Gamma_{bra} &= \begin{bmatrix} 0 & 0 & 0 & 0 \end{bmatrix}^T, & \Theta_{bra} &= \begin{bmatrix} 0 & 0 & 0 & -1 \end{bmatrix}^T \\
\Gamma_{ebr} &= \begin{bmatrix} 0 & 0 & 0 & 0 \end{bmatrix}^T, & \Theta_{ebr} &= \begin{bmatrix} 0 & -1 & 0 & 0 \end{bmatrix}^T \\
\Gamma_{hvb} &= \begin{bmatrix} 0 & 0 & 0 & 0 \end{bmatrix}^T, & \Theta_{hvb} &= \begin{bmatrix} 0 & -1 & 0 & 0 \end{bmatrix}^T
\end{aligned} \tag{2-3}$$

Chapter 3

Speed-Torque Coupled MEMS

Considering speed as an optimization variable in ECMS is a relatively uncharted research territory. Select literature exist for this approach such as the work in [10]. However, the approach is not based modularity/distributed control and the focus is on finding an optimal equivalent factor. The optimization is performed using a Genetic Algorithm, which can increase the computational cost when performed without modularity.

Machine learning-based velocity prediction is used in many EMS approaches. A relevant example is shown in [3], where velocity prediction is used for energy prediction along with A-ECMS to update the EF. The flexible adjustment of EF has ensured desirable results in terms of fuel economy and SOC sustainability.

In [4], the optimal power split and gear shift is determined by using an actor-gear-critic based DP and then a multi-stage neural network prediction layer is used for velocity prediction. In this approach, the optimal power split is found along with the optimal gear shift strategy by solving a mixed-integer problem. It is shown that the algorithm achieves results close to DP in terms fuel economy, despite not taking the entire driving cycle into account, which is desirable.

In general, A-ECMS with neural network based velocity prediction is shown to achieve 3% better fuel economy than A-ECMS without prediction as per [16]. However, in the MEMS approach, an increase in computational cost is possible on adding a neural network prediction layer to each subsystem. It is important to note that these methods predict the velocity of the vehicle and not the speed of the subsystems. Also, prediction of velocity and driving cycle does not ensure optimal operating speeds of the subsystem and thus, these approaches are cannot be applied in cases where optimal operating speeds of the subsystems need to be found.

When speed of subsystems are considered in the OCP seen in the previous section, the OCP will change to incorporate the new optimization variable(s). The constraints in Equation (1-6) are affected

as the coefficients in these equations are dependent on the speed of the subsystems as shown in Equation (1-7).

3-1 Power Loss Functions

As mentioned in [11], the input-output power losses are approximated as polynomial functions with speed-dependent coefficients. Currently, these coefficients are approximated using a look-up table approach. The input-output power is measured for different speeds and torques. Then, for each different speed, depending on the measured input-output power, a polynomial function in the form of Equation (1-6) is fitted. This approach with the look-up table is shown in Figure 3-1, where k values of torque (T) and speed(ω) are taken, an input-output power ($u-y$) measurement is taken. This is performed for all subsystems which involve mechanical energy, namely, ICE, MG1 and MG2 etc. For other subsystems the coefficients are not speed-dependent.

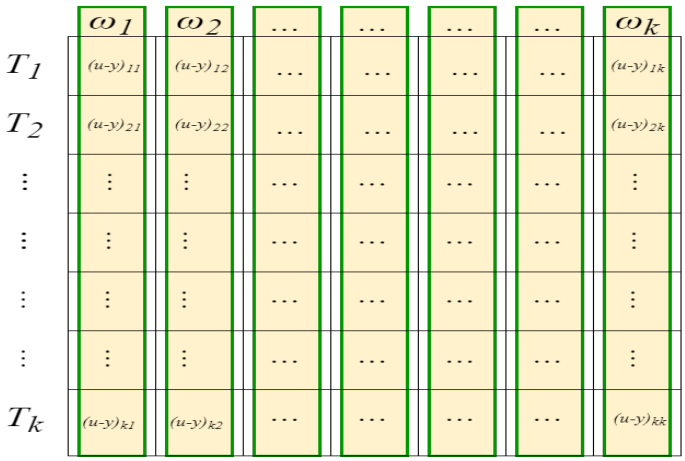

Figure 3-1: Look-up Table for finding the Polynomial Function

For the subsystems for which the input-output power constraint is speed dependent, Equation (1-6) is changed according to Equation (1-7) as :

$$\underbrace{y_{m,k}+\frac{1}{2}q_{m,k}(\omega_{m,k})u_{m,k}^2+f_{m,k}(\omega_{m,k})u_{m,k}+e_{m,k}(\omega_{m,k})=0}_{f_{constraint}(\omega_{m,k},u_{m,k},y_{m,k})} \tag{3-1}$$

$\forall\, m \in \mathscr{M}$ corresponding to ICE, EM, $k \in \mathscr{K}$

As the speed is unknown, the functions $q_{m,k}(\omega_{m,k})$, $f_{m,k}(\omega_{m,k})$ and $e_{m,k}(\omega_{m,k})$ have to be estimated with respect to $\omega_{m,k}$. For this purpose, the raw data for the subsystems speed and the coefficients are obtained and least squares fitting is performed. The data is split into training and validation in a 2:1 ratio. To ensure uniformity of samples, the data is sorted from low to high speed and the first and second two samples are given for the training and every third sample is given for validation. The

fitting is done for the training set and the results are analyzed using the validation set. For the fitting, quadratic, cubic, 4-degree, 5-degree, 6-degree polynomials and exponential functions are tried. The function with the highest VAF is selected. If there are multiple functions with VAF greater than 90%, the least VAF greater than 90% is selected. This criteria differs for exponential fitting because its negligence may interfere with the inherent physics of the system/subsystem.

A point to be noted is that MG1 has different dynamics in the positive power region and negative power region. As speed ω is always considered positive, the sign or direction of the power is decided by that of the torque. Thus, there are two different coefficient datasets for the negative and positive torque/power directions.

Coefficient	Best Function Fit	Validation VAF (%)
q_{ice}	6-degree	91.26
f_{ice}	6-degree	68.95
e_{ice}	Quadratic	97.30
$q_{mg1,+}$	Exponential	63.75
$f_{mg1,+}$	5-degree	95.83
$e_{mg1,+}$	Quadratic	96.13
$q_{mg1,-}$	Exponential	68.18
$f_{mg1,-}$	6-degree	90.61
$e_{mg1,-}$	Quadratic	94.97

Table 3-1: Fitting Results for coefficients q, f, e vs speed ω

The fitting results are plotted as below.

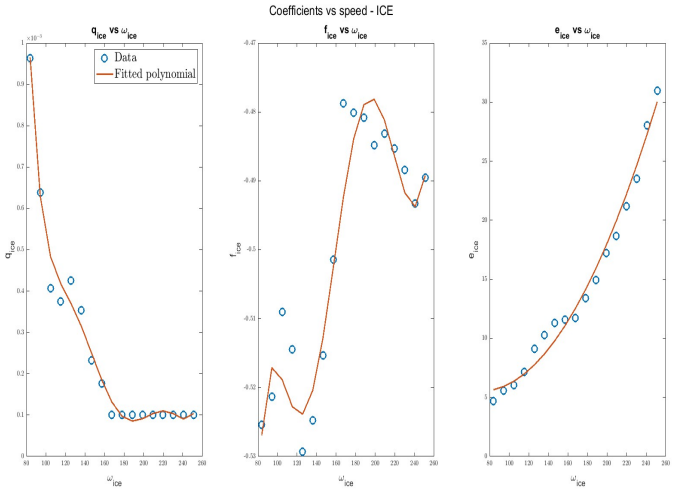

Figure 3-2: Coefficients vs speed - ICE

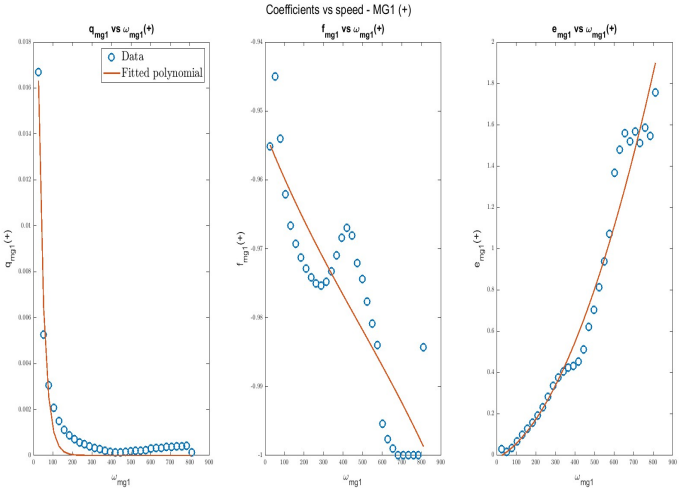

Figure 3-3: Coefficients vs speed - MG1 - Positive Torque

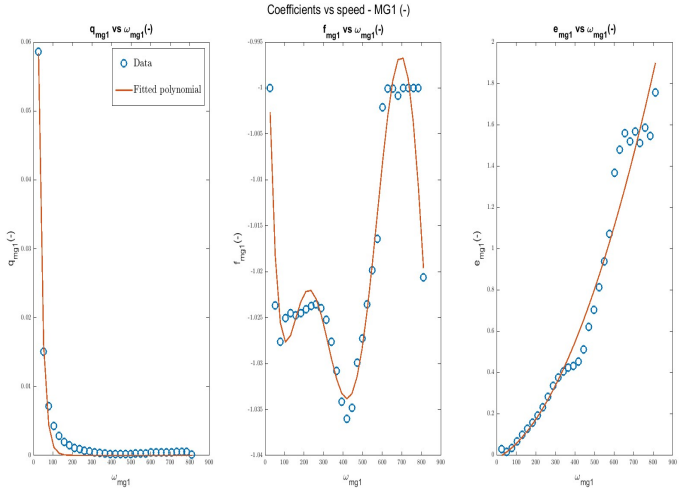

Figure 3-4: Coefficients vs speed - MG1 - Negative Torque

Despite the high VAFs for most function selections, these functions will have to be multiplied with quadratic and linear terms of input power $u_{m,k}$, which is another optimization variable. Thus, the degree of this constraint increases and cross-terms between $\omega_{m,k}$ and $u_{m,k}$ are added. This introduces non-convexity, which makes the algorithm lose the optimality guarantee could vastly increase the computational time of the optimization.

Thus, a different method to perform the data fitting between input, output power and subsystem speed is explored. The attempt is to keep this constraint quadratic so that it is computationally inexpensive.

The constraint is then replaced with a new quadratic power loss constraint where the power loss P_{loss} or Δu is represented in terms of speed ω of subsystems ICE and MG1. Here, the fact that an input

power received by a subsystem disperses as output power and power loss is used. To examine the behaviour of power loss and speed, the raw data for input, output power and speed data are collected and power loss ($u_{ice} - y_{ice}$) is plotted for ICE compared to the speed of ICE (ω_{ice}).

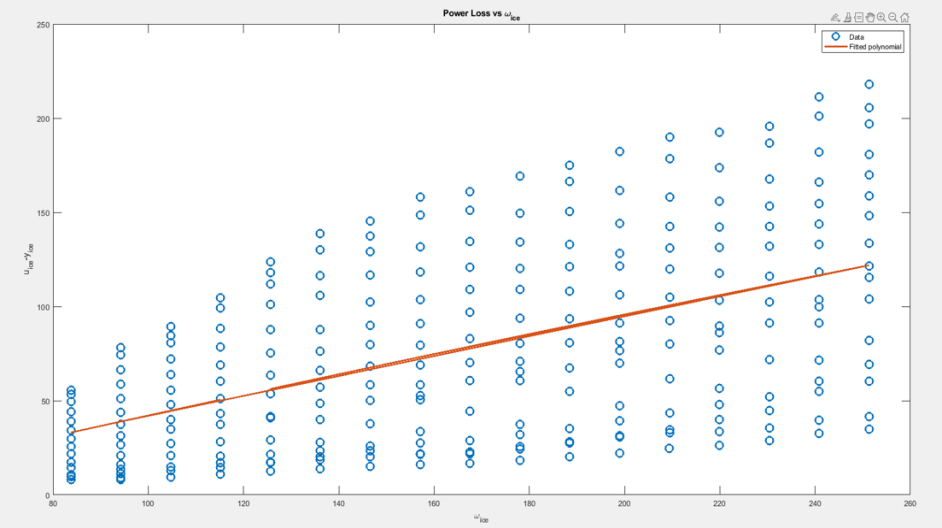

Figure 3-5: Power Loss vs speed - ICE

The plot in Figure 3-5 clearly indicates a one-to-many mapping between speed and power loss. This arises due to the dependence on torque as well. Thus, torque should also be treated as an optimization variable along with speed and power and the power loss P_{loss} is represented in terms of speed and torque of subsystems ICE and MG1.

Thus, for $m \in \{ICE, MG1\}$,

$$u_{m,k} - y_{m,k} - P_{loss}(\omega_{m,k}, \tau_{m,k}) = 0 \tag{3-2}$$

where P_{loss} is a power loss function fitted in terms of $\omega_{m,k}$ and $\tau_{m,k}$ according to the fit types given in the below equation.

$$\begin{aligned}
&\text{Fit Type 1}: P_{loss}(\omega_{m,k}, \tau_{m,k}) = A_m + B_m\omega_{m,k} + C_m\tau_{m,k} + D_m\omega_{m,k}^2 + E_m\tau_{m,k}^2 + F_m\omega_{m,k}\tau_{m,k} \\
&\text{Fit Type 2}: P_{loss}(\omega_{m,k}, \tau_{m,k}) = B_m\omega_{m,k} + C_m\tau_{m,k} + D_m\omega_{m,k}^2 + E_m\tau_{m,k}^2 + F_m\omega_{m,k}\tau_{m,k} \\
&\text{Fit Type 3}: P_{loss}(\omega_{m,k}, \tau_{m,k}) = D_m\omega_{m,k}^2 + E_m\tau_{m,k}^2 \\
&\text{Fit Type 4}: P_{loss}(\omega_{m,k}, \tau_{m,k}) = B_m\omega_{m,k} + C_m\tau_{m,k}
\end{aligned} \tag{3-3}$$

$\forall\, m \in \{ICE, MG1\}, k \in \mathscr{K}$

To perform the fitting, the raw dataset for input and output power u and y, speed ω and torque τ are collected for $m \in \{\text{ICE}, \text{EMS}\}$ and $k \in \mathscr{K}$. The power loss data $\Delta u_{m,k}$ is given by -

$$\Delta u_{m,k} = u_{m,k} - y_{m,k} \tag{3-4}$$

for $m \in \{\text{ICE}, \text{EMS}\}$ and $k \in \mathscr{K}$.

The method used for data fitting is linear least squares whose method is derived for Type 1 as :

$$\underbrace{\begin{bmatrix} \Delta u_{m,1} \\ . \\ . \\ . \\ \Delta u_{m,k} \end{bmatrix}}_{\Delta U_m} = \underbrace{\begin{bmatrix} 1 & \omega_{m,1} & \tau_{m,1} & \omega_{m,1}^2 & \tau_{m,1}^2 & \omega_{m,1} * \tau_{m,1} \\ . & & & & & \\ . & & & & & \\ . & & & & & \\ 1 & \omega_{m,k} & \tau_{m,k} & \omega_{m,k}^2 & \tau_{m,k}^2 & \omega_{m,k} * \tau_{m,k} \end{bmatrix}}_{X_m} \underbrace{\begin{bmatrix} A_m \\ B_m \\ C_m \\ D_m \\ E_m \\ F_m \end{bmatrix}}_{\Theta_m} + \underbrace{\begin{bmatrix} \varepsilon_1 \\ . \\ . \\ . \\ \varepsilon_k \end{bmatrix}}_{\varepsilon_m} \tag{3-5}$$

$$\Delta U_m = X_m \Theta_m + \varepsilon_m$$

The coefficient matrix Θ_m is found by minimizing the 2-norm of the error term ε_m as follows.

$$\hat{\Theta}_m = \arg\min_{\Theta_m} ||\Delta U_m - X_m \Theta_m||_2^2 \tag{3-6}$$

Using the estimated coefficients, the predicted model of the power loss $\Delta\hat{U}_m$ is obtained.

$$\begin{gathered} \Delta\hat{U}_m = X_m \hat{\Theta}_m \\ \Delta\hat{u}_{m,i} = \begin{bmatrix} 1 & \omega_{m,i} & \tau_{m,i} & \omega_{m,i}^2 & \tau_{m,i}^2 & \omega_{m,i}\tau_{m,i} \end{bmatrix} \hat{\Theta}_m \; \forall \; m \in \{\text{ICE,MG1}\} \text{ and } i \in \mathscr{K} \end{gathered} \tag{3-7}$$

The Δu, ω and τ data is divided into training and validation sets in a 2:1 ratio where the first two samples are given for the training and the third sample is given for validation. This training data for P_{loss} is then fitted as functions of $\omega_{m,k}$ and $\tau_{m,k}$ using least-squares fitting an in all fit types as seen in Equation 3-3. The fitting results for each type are tabulated with respect to VAF for the validation set as in Table 3-2. The VAF is calculated by :

$$VAF = (1 - \frac{\sum_{i \in \mathscr{K}} \Delta\hat{u}_{m,i} - \Delta u_{m,i}}{\sum_{i \in \mathscr{K}} \Delta\hat{u}_{m,i} - \bar{\Delta u}_m})\text{x}100\% \tag{3-8}$$

where $\bar{\Delta u}_m$ is the mean of the power loss data.

An important note to be considered is that the predicted power loss $\Delta\hat{u}$ is derived by using the estimated coefficients on the validation dataset given in the equation as Δu. Although the above least-squares is derived for Fit Type 1, the same method is used for Types 2,3 and 4. Also, the function mapping is performed separately for positive and negative torque regions for MG1.

Subsystem	Validation VAF (%)			
	Fit Type 1	Fit Type 2	Fit Type 3	Fit Type 4
ICE	99.59	99.51	85.58	81.65
MG1 (+)	95.71	95.26	76.59	68.80
MG1 (-)	94.85	94.32	76.62	67.26

Table 3-2: VAF Results for Validation Data for all Fit Types

To further examine the best fit type, the coefficients for each fit type are tabulated in Table 3-3, Table 3-4 and Table 3-5. These coefficients are the elements of the Θ matrices in Equation 3-5.

Fit Type	A_m	B_m	C_m	D_m	E_m	F_m
Fit Type 1	20815.19	-273.3	0.1994	1.747	0.01781	1.154
Fit Type 2	-	-30.95	15.17	1.087	0.006867	1.102
Fit Type 3	-	-	-	1.534	0.3045	-
Fit Type 4	-	248.5	168.3	-	-	-

Table 3-3: Coefficients in each Fit Type for ICE

Fit Type	A_m	B_m	C_m	D_m	E_m	F_m
Fit Type 1	885.4	-4.406	-6.98	0.00649	0.04004	0.05085
Fit Type 2	-	-1.632	-0.9561	0.004356	0.02925	0.04415
Fit Type 3	-	-	-	0.007566	0.06371	-
Fit Type 4	-	3.763	14.63	-	-	-

Table 3-4: Coefficients in each Fit Type for MG1(+)

Fit Type	A_m	B_m	C_m	D_m	E_m	F_m
Fit Type 1	1035	-5.217	7.06	0.007032	0.03863	-0.05274
Fit Type 2	-	-2.436	-0.6057	0.005055	0.02436	-0.04536
Fit Type 3	-	-	-	0.008029	0.06203	-
Fit Type 4	-	4.024	-14.34	-	-	-

Table 3-5: Coefficients in each Fit Type for MG1(-)

To decide the final fit type, the VAF is first considered. For fit type 1 and 2, the VAFs are close to 95% and almost similar. While examining the coefficients of fit type 1 and 2, the constant coefficient A_m is of a higher order compared to the other coefficients. Thus, it is possible that the high constant term could lead to overfitting of the data to this constant term and reduce the weight and dependency on the optimization variables $\omega_{m,k}$ and $\tau_{m,k}$. Thus, fit type 2 is considered as the final fit type and the data fitting is plotted in Figure 3-6a, Figure 3-6b and Figure 3-6c.

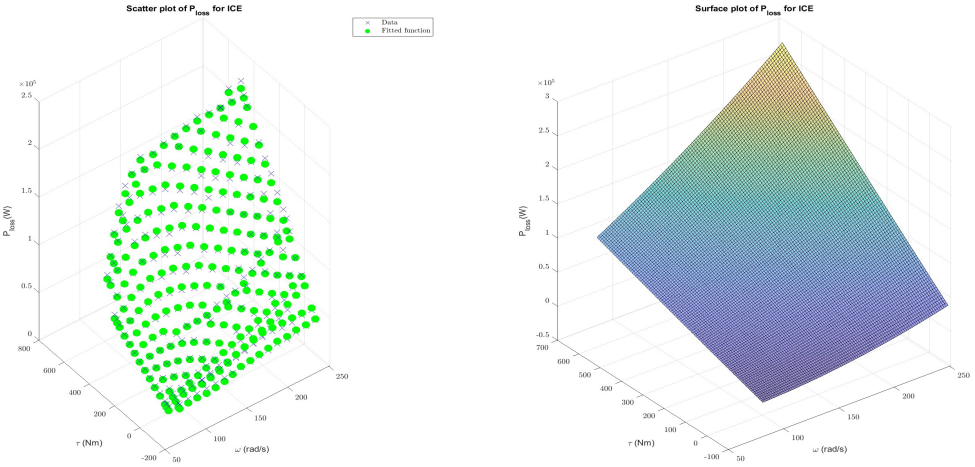

(a) ICE

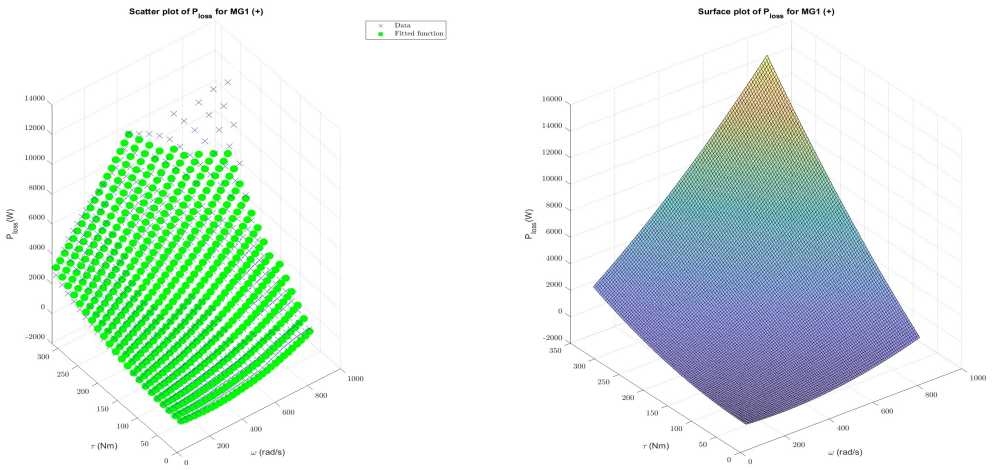

(b) MG1 (+)

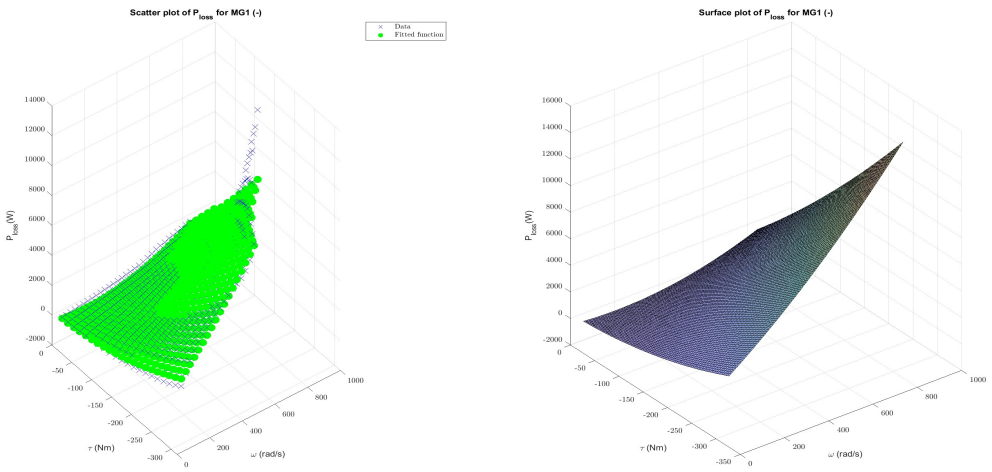

(c) MG1 (-)

Figure 3-6: Power Loss vs speed and torque

Another issue with including subsystem speed and torque as a decision variable for ICE and MG1 is that the subsystems are mechanically connected through a fixed-ratio gearset. The fixed gear ratio is 3. Thus, their speeds and torques are dependent as :

$$\begin{aligned} 3\omega_{ice,k} - \omega_{mg1,k} &= 0 \\ \frac{1}{3}\tau_{ice,k} + \tau_{mg1,k} &= 0 \end{aligned} \tag{3-9}$$

$\forall k \in \mathscr{K}$

Since this constraint also involves multiple subsystems, it is best to approach this in the same way as the connection constraint in Equation 1-9. They can be treated as nodes where speeds and torques are connected. Thus, these constraints will be penalized and added to the objective function as :

$$\min_{u_m, y_m, \omega_m, \tau_m} \sum_{m \in \mathscr{M}} \sum_{k \in \mathscr{K}} c_m u_{m,k} - d_m y_{m,k} + \mu_{1,k}^T (\Gamma_m u_{m,k} + \Theta_m y_{m,k} + \frac{1}{M} v_k) + \mu_{2,k}(\Omega_m \omega_{m,k}) + \mu_{3,k}(\Lambda_m \tau_{m,k}) \tag{3-10}$$

where,

$$\begin{aligned} \Omega_{ice} &= 3, & \Lambda_{ice} &= -1 \\ \Lambda_{mg1} &= \frac{1}{3}, & \Lambda_{mg1} &= 1 \end{aligned} \tag{3-11}$$

and $\mu_1 \in \mathbb{R}^N$, $\mu_2 \in \mathbb{R}$ and $\mu_3 \in \mathbb{R}$ are Lagrangian variables used to penalize the interconnectivity constraints and the gearbox constraints. For the remaining subsystems, the Ω and Λ values shall be 0.

The subsystem speed and torque can be bounded and these constraints can be added.

$$\begin{aligned} \underline{\omega} \leq \omega_{m,k} \leq \bar{\omega} \\ \underline{\tau} \leq \tau_{m,k} \leq \bar{\tau} \end{aligned} \tag{3-12}$$

$\forall\, m \in \{\text{ICE}, \text{MG1}\}, k \in \mathscr{K}$ and $\underline{\omega}$, $\bar{\omega}$, $\underline{\tau}$ and $\bar{\tau}$ are constant bound for subsystem speed and torque.

Since speed and torque are decision variables and the output from ICE and input to MG1 is mechanical energy, it is important that the powers follow the power formula. Thus,

$$y_{m,k} = \omega_{m,k} \tau_{m,k} \tag{3-13}$$

$\forall\, m = \{\text{ICE}, \text{MG1}\}, k \in \mathscr{K}$

The above equation is used to modify the objective function for ICE and MG1.

3-1-1 Alternate Formulation

For $m = \{\text{ICE}, \text{MG1}\}$. Substituting $y_{m,k} = \omega_{m,k}\tau_{m,k}$ in the power loss constraint in Equation 3-2,

$$\begin{aligned} -u_{m,k} + \omega_{m,k}\tau_{m,k} + B_m\omega_{m,k} + C_m\tau_{m,k} + D_m\omega_{m,k}^2 + E_m\tau_{m,k}^2 + F_m\omega_{m,k}\tau_{m,k} = 0 \\ u_{m,k} = \underbrace{\omega_{m,k}\tau_{m,k}}_{y_{m,k}} + \underbrace{B_m\omega_{m,k} + C_m\tau_{m,k} + D_m\omega_{m,k}^2 + E_m\tau_{m,k}^2 + F_m\omega_{m,k}\tau_{m,k}}_{P_{loss}(\omega_{m,k},\tau_{m,k})} \end{aligned} \tag{3-14}$$

Substituting the expression for $u_{m,k}$ in the objective function,

$$\begin{aligned} &\sum_{k\in\mathscr{K}} c_m u_{m,k} - d_m y_{m,k} + \mu_{1,k}^T(\Gamma_m u_{m,k} + \Theta_m y_{m,k} + \underbrace{\frac{1}{M}v_k}_{\text{constant w.r.t subsystem m}}) + \mu_{2,k}(\Omega_m\omega_{m,k}) + \mu_{3,k}(\Lambda_m\tau_{m,k}) \\ &= \sum_{k\in\mathscr{K}} (c_m + \underbrace{\mu_{1,k}^T\Gamma}_{\mu_{u,k}})u_{m,k} - (d_m - \underbrace{\mu_{1,k}^T\Theta_m}_{\mu_{y,k}})y_{m,k} + \mu_{2,k}(\Omega_m\omega_{m,k}) + \mu_{3,k}(\Lambda_m\tau_{m,k}) \\ &= \sum_{k\in\mathscr{K}} (c_m + \mu_{u,k})(\omega_{m,k}\tau_{m,k} + B_m\omega_{m,k} + C_m\tau_{m,k} + D_m\omega_{m,k}^2 + E_m\tau_{m,k}^2 + F_m\omega_{m,k}\tau_{m,k}) \\ &-(d_m - \mu_{y,k})(\omega_{m,k}\tau_{m,k}) + \mu_{2,k}(\Omega_m\omega_{m,k}) + \mu_{3,k}(\Lambda_m\tau_{m,k}) \\ &= \sum_{k\in\mathscr{K}} (c_m + \mu_{u,k})D_m\omega_{m,k}^2 + (c_m + \mu_{u,k})E_m\tau_{m,k}^2 + ((c_m + \mu_{u,k})(F_m + 1) - d_m + \mu_{y,k}))\omega_{m,k}\tau_{m,k} \\ &\quad + ((c_m + \mu_{u,k})B_m + \mu_{2,k}\Omega_m)\omega_{m,k} + ((c_m + \mu_{u,k})C_m + \mu_{3,k}\Lambda_m)\tau_{m,k} \\ &\quad = \sum_{k\in\mathscr{K}} \begin{bmatrix}\omega_{m,k} & \tau_{m,k}\end{bmatrix} \underbrace{\begin{bmatrix} (c_m + \mu_{u,k})D_m & \frac{1}{2}((c_m + \mu_{u,k})(F_m + 1) - d_m + \mu_{y,k}) \\ \frac{1}{2}((c_m + \mu_{u,k})(F_m + 1) - d_m + \mu_{y,k}) & (c_m + \mu_{u,k})E_m \end{bmatrix}}_{Q_{m,k}} \begin{bmatrix}\omega_{m,k} \\ \tau_{m,k}\end{bmatrix} \\ &\quad + \underbrace{\begin{bmatrix}((c_m + \mu_{u,k})B_m + \mu_{2,k}\Omega_m) & ((c_m + \mu_{u,k})C_m + \mu_{3,k}\Lambda_m)\end{bmatrix}}_{q_{m,k}} \begin{bmatrix}\omega_{m,k} \\ \tau_{m,k}\end{bmatrix} \\ &\quad = \sum_{k\in\mathscr{K}} \begin{bmatrix}\omega_{m,k} & \tau_{m,k}\end{bmatrix} Q_{m,k} \begin{bmatrix}\omega_{m,k} \\ \tau_{m,k}\end{bmatrix} + q_{m,k} \begin{bmatrix}\omega_{m,k} \\ \tau_{m,k}\end{bmatrix} \end{aligned} \tag{3-15}$$

Thus, the OCP will now be,

$$\begin{aligned} \min_{\omega_{m,k},\tau_{m,k}} &\sum_{k\in\mathscr{K}} \begin{bmatrix}\omega_{m,k} & \tau_{m,k}\end{bmatrix} Q_{m,k} \begin{bmatrix}\omega_{m,k} \\ \tau_{m,k}\end{bmatrix} + q_{m,k} \begin{bmatrix}\omega_{m,k} \\ \tau_{m,k}\end{bmatrix} \\ \text{s.t. } &\underline{\omega} \le \omega_{m,k} \le \bar{\omega} \\ &\underline{\tau} \le \tau_{m,k} \le \bar{\tau} \end{aligned} \tag{3-16}$$

This can be solved as a quadratic programming problem. If the matrix $Q_{m,k}$ is positive definite, then

this problem is convex.

Assuming the solution to the above OCP is derived as $\begin{bmatrix}\omega^*_{m,k}\\ \tau^*_{m,k}\end{bmatrix}$, the power output is then,

$$\begin{aligned} y^*_{m,k} &= \omega^*_{m,k}\tau^*_{m,k} \\ u^*_{m,k} &= \omega^*_{m,k}\tau^*_{m,k} + B_m\omega^*_{m,k} + C_m\tau^*_{m,k} + D_m\omega^{*2}_{m,k} + E_m\tau^{*2}_{m,k} + F_m\omega^*_{m,k}\tau^*_{m,k} \end{aligned} \tag{3-17}$$

Conditions for Positive Definiteness

The matrix $Q_{m,k}$ needs to be positive definite to preserve convexity and obtain a solution. Since $Q_{m,k}$ is 2x2 symmetric matrix, it is known that for positive definiteness, the following 2 conditions need to be satisfied :

(i) $tr(Q_{m,k}) > 0$

(ii) $det(Q_{m,k}) > 0$

For trace condition,

$$\begin{aligned} & tr(Q_{m,k}) > 0 \\ & (c_m + \mu_{u,k})D_m + (c_m + \mu_{u,k})E_m > 0 \\ & (c_m + \mu_{u,k})(D_m + E_m) > 0 \\ & \text{if } (D_m + E_m) > 0, \text{ then } \mu_{u,k} > -c_m \\ & \text{if } (D_m + E_m) < 0, \text{ then } \mu_{u,k} < -c_m \end{aligned} \tag{3-18}$$

For determinant condition,

$$\begin{aligned} & det(Q_{m,k}) > 0 \\ & (c_m + \mu_{u,k})^2 D_m E_m - \frac{1}{4}((c_m + \mu_{u,k})(F_m + 1) - d_m + \mu_{y,k})^2 > 0 \\ & 4(c_m + \mu_{u,k})^2 D_m E_m > ((c_m + \mu_{u,k})(F_m + 1) - d_m + \mu_{y,k})^2 \\ & ((c_m + \mu_{u,k})(F_m + 1) - d_m + \mu_{y,k})^2 < 4(c_m + \mu_{u,k})^2 D_m E_m \end{aligned} \tag{3-19}$$

This condition can be divided into 2 parts.

$$\begin{array}{c|c} (c_m + \mu_{u,k})(F_m + 1) - d_m + \mu_{y,k} < 2(c_m + \mu_{u,k})(D_m E_m)^{\frac{1}{2}} & (c_m + \mu_{u,k})(F_m + 1) - d_m + \mu_{y,k} > -2(c_m + \mu_{u,k})(D_m E_m)^{\frac{1}{2}} \\ (F_m + 1) - \frac{(d_m - \mu_{y,k})}{(c_m + \mu_{u,k})} < 2(D_m E_m)^{\frac{1}{2}} & (F_m + 1) - \frac{(d_m - \mu_{y,k})}{(c_m + \mu_{u,k})} > -2(D_m E_m)^{\frac{1}{2}} \\ \frac{(d_m - \mu_{y,k})}{(c_m + \mu_{u,k})} > (F_m + 1) - 2(D_m E_m)^{\frac{1}{2}} & \frac{(d_m - \mu_{y,k})}{(c_m + \mu_{u,k})} < (F_m + 1) + 2(D_m E_m)^{\frac{1}{2}} \end{array}$$

Thus, in conclusion, the conditions for positive definiteness are derived as,

$$(F_m + 1) - 2(D_m E_m)^{\frac{1}{2}} < \frac{(d_m - \mu_{y,k})}{(c_m + \mu_{u,k})} < (F_m + 1) + 2(D_m E_m)^{\frac{1}{2}} \tag{3-20}$$

Thus, the Lagrangian variables μ_u and μ_y are tuned in order to make the problem convex.

Input Power Bounds

Defining bounds the subsystem speed and torque eliminates the need for power bound constraint in Equation 1-8. Since input power depends on subsystem speed and torque as seen in Equation 3-14, the power bounds should also depend on the bounds of speed and torque.

By using Equation 3-14, the input power bounds are derived as follows -

$$\begin{aligned}
\underline{y}_{m,k} &= min(\underline{\omega}\,\underline{\tau},\ \underline{\omega}\bar{\tau},\ \bar{\omega}\underline{\tau},\ \bar{\omega}\bar{\tau}) \\
\bar{y}_{m,k} &= max(\underline{\omega}\,\underline{\tau},\ \underline{\omega}\bar{\tau},\ \bar{\omega}\underline{\tau},\ \bar{\omega}\bar{\tau}) \\
\underline{u}_{m,k} &= min(\underline{\omega}\,\underline{\tau}+P_{loss}(\underline{\omega},\underline{\tau}),\ \underline{\omega}\bar{\tau}+P_{loss}(\bar{\omega},\underline{\tau}),\ \bar{\omega}\underline{\tau}+P_{loss}(\bar{\omega},\underline{\tau}),\ \bar{\omega}\bar{\tau}+P_{loss}(\bar{\omega},\bar{\tau})) \\
\bar{u}_{m,k} &= max(\underline{\omega}\,\underline{\tau}+P_{loss}(\underline{\omega},\underline{\tau}),\ \underline{\omega}\bar{\tau}+P_{loss}(\bar{\omega},\underline{\tau}),\ \bar{\omega}\underline{\tau}+P_{loss}(\bar{\omega},\underline{\tau}),\ \bar{\omega}\bar{\tau}+P_{loss}(\bar{\omega},\bar{\tau}))
\end{aligned} \tag{3-21}$$

Thus, after calculating the optimal power as in Equation 3-17, the input and output optimal power are saturated to the above defined bounds.

Lagrangian Updates

Since 2 additional Lagrangian variables μ_2 and μ_3 are introduced in the new OCP, they also need to be updated using a gradient ascent as seen in Equation 1-18 for every iteration s. Thus, the Lagrangian update is done as follows :

$$\begin{aligned}
\mu_{1,k}^{s+1} &= \mu_{1,k}^{s} + \alpha_{1,k}^{s} \sum_{m\in\mathscr{M}} (\Gamma_m u_{m,k}^{s} + \Theta_m y_{m,k}^{s} + \frac{1}{M} v_k) \\
\mu_{2,k}^{s+1} &= \mu_{2,k}^{s} + \alpha_{2,k}^{s} \sum_{m\in\mathscr{M}} (\Omega_m \omega_{m,k}) \\
\mu_{3,k}^{s+1} &= \mu_{3,k}^{s} + \alpha_{3,k}^{s} \sum_{m\in\mathscr{M}} (\Lambda_m \tau_{m,k})
\end{aligned} \tag{3-22}$$

For stepsize α_1, the update is performed with a Newton Scheme as mentioned in [12] and it is unchanged from the current implementation of MEMS. For stepsizes α_2 and α_3, constant stepsize values are chosen.

Other Subsystems

For other subsystems, the OCP is the same as the original MEMS as shown in Equation 1-17 and the Lagrangian update is performed as per Equation 1-18. The additional Lagrangian variables μ_2, μ_3 and coefficients Ω, Λ for these subsystems are set as 0.

3-2 Revised Algorithm

The original MEMS is revised to accommodate speed of ICE and MG1 using the same partial Lagrangian approach as in Equation 1-12.

$$g(\mu_{1,k},\mu_{2,k},\mu_{3,k}) = \mu_{1,k}^T v_k + g_m(\{\mu_{1,k},\mu_{2,k},\mu_{3,k}\}) \tag{3-23}$$

where for $m = \{\text{ICE},\text{MG1}\}$ is taken from Equation 3-16,

$$\begin{aligned} g_m(\{\mu_{1,k},\mu_{2,k},\mu_{3,k}\}) = \min_{\omega_{m,k},\tau_{m,k}} \sum_{k\in\mathscr{K}} & \begin{bmatrix}\omega_{m,k} & \tau_{m,k}\end{bmatrix} Q_{m,k} \begin{bmatrix}\omega_{m,k}\\ \tau_{m,k}\end{bmatrix} + q_{m,k}\begin{bmatrix}\omega_{m,k}\\ \tau_{m,k}\end{bmatrix} \\ \text{s.t. } & \underline{\omega} \le \omega_{m,k} \le \bar{\omega} \\ & \underline{\tau} \le \tau_{m,k} \le \bar{\tau} \end{aligned} \tag{3-24}$$

and,

$$\begin{aligned} y^*_{m,k} &= \omega^*_{m,k}\tau^*_{m,k} \\ u^*_{m,k} &= \omega^*_{m,k}\tau^*_{m,k} + B_m\omega^*_{m,k} + C_m\tau^*_{m,k} + D_m\omega^{*2}_{m,k} + E_m\tau^{*2}_{m,k} + F_m\omega^*_{m,k}\tau^*_{m,k} \end{aligned} \tag{3-25}$$

For $m = \{\text{HVB}\}$,

$$\begin{aligned} g_{hvb}(\mu_{1,k}) = \min_{\{u_{hvb,k},y_{hvb,k}\}} \sum_{k\in\mathscr{K}} & (c_{hvb} + \mu_{1,k}^T\Gamma_{hvb})u_{hvb,k} - (d_{hvb} - \mu_{1,k}^T\Theta_{hvb})y_{hvb,k} + \lambda_k u_{hvb,k} \\ \text{s.t. } & \underline{u}_{hvb,k} \le u_{hvb,k} \le \bar{u}_{hvb,k} \\ & y_{hvb,k} + \frac{1}{2}q_{hvb,k}u^2_{hvb,k} + f_{hvb,k}u_{hvb,k} + e_{hvb,k} = 0 \\ & x_{hvb,k+1} = A_{hvb}x_{hvb,k} + B_{hvb,w}w_{hvb,k} + B_{hvb,u}u_{hvb,k} \\ & \underline{x}_{hvb,k} \le x_{hvb,k} \le \bar{x}_{hvb,k} \end{aligned} \tag{3-26}$$

For $m \in \mathscr{M}\backslash\{\text{ICE},\text{MG1},\text{HVB}\}$

$$\begin{aligned} g_m(\mu_{1,k}) = \min_{\{u_{m,k},y_{m,k}\}} \sum_{k\in\mathscr{K}} & (c_m + \mu_{1,k}^T\Gamma_m)u_{m,k} - (d_m - \mu_{1,k}^T\Theta_m)y_{m,k} \\ \text{s.t. } & \underline{u}_{m,k} \le u_{m,k} \le \bar{u}_{m,k} \\ & y_{m,k} + \frac{1}{2}q_{m,k}u^2_{m,k} + f_{m,k}u_{m,k} + e_{m,k} = 0 \end{aligned} \tag{3-27}$$

The revised MEMS is from now referred to as ST-MEMS and can be summarized in the following

algorithm where $\varepsilon > 0$ is a well chosen convergence criteria, $s \in \{0, \ldots, s_{\max}\}$ is the iteration counter and $s_{\max}$ is the maximum number of iterations.

Algorithm

At time instant $k \in \mathscr{K}$, for a given λ_k, initialize $\mu^0_{1,k}$, set $\varepsilon > 0, s_{\max} > 1$.

- Measure $x_{hvb,k}$ and v_k
- While $\left\|\mu^{s+1}_{1,k} - \mu^s_{1,k}\right\| \geq \varepsilon$ or $\left\|\mu^{s+1}_{2,k} - \mu^s_{2,k}\right\| \geq \varepsilon$ or $\left\|\mu^{s+1}_{3,k} - \mu^s_{3,k}\right\| \geq \varepsilon$ or $s < s_{\max}$
  - Solve Equation 3-23
  - Update the Lagrangian dual variables using Equation 3-22 to find the optimal Lagrangian values $\mu^*_{1,k}$, $\mu^*_{2,k}$, $\mu^*_{3,k}$.
- Initialize the dual variables at $k+1$ with the optimal dual variables at time instant k, i.e., $\mu^0_{1,k+1} = \mu^*_{1,k}$ and $\mu^0_{2,k+1} = \mu^*_{2,k}$ and $\mu^0_{3,k+1} = \mu^*_{3,k}$.

Chapter 4

Results and Discussions

In this chapter, the MEMS and the ST-MEMS are run for different cases where the inputs are adjusted and the performance of each algorithm is analyzed. The advantages and disadvantages of the ST-MEMS are then summarized. Based on the disadvantages, an alternate approach is suggested and future work is proposed to improve the algorithm.

4-1 Simulation Results

The simulation is carried out in open-loop similar to the case in the original MEMS as described in [13]. The entire vehicle model is not considered at first as it contains several other components and their control systems such as Battery Management System (BMS) which controls the equivalent factor (EF). Since these act in a feedback loop, these affect the MEMS algorithm. To evaluate the results of the MEMS, only that particular algorithm is tested. All simulations are performed in MATLAB/Simulink.

The inputs to the MEMS block of Simulink are given below :

- The exogenous inputs v_1, v_2, v_3, v_4 (in kW) where,
  - v_1 is the power to the Hydraulic Pump (HP)
  - v_2 is the power to the eAUX

  - v_3 is the power out of the gearbox assumed to be zero
  - v_4 is the power demand to the drive. This is an important input as this power demand must be satisfied by the output power of MG2 ($y_{mg2} \simeq v_4$) for the series-hybrid wheel loader case.

- The bounds for the subsystem speed and torque $\underline{\omega}$, $\bar{\omega}$, $\underline{\tau}$, $\bar{\tau}$ for ICE and MG1. The bounds for ω are in rad/s and that of τ are in Nm.
- State-of-Charge (SOC)% to the HVB
- equivalent factor (EF) λ
- The variables which decide the q, f, e coefficients in Equation 1-7 such the speed of MG2 (ω_{mg2}), SOC, temperature of the EBR and gear number.
- In case of the MEMS algorithm, the speed for ICE needs to be an input and the speed for MG1 is 3 times the speed of ICE.

The simulations are performed for a number of cases by varying some of the above mentioned inputs and performances are compared for both MEMS and ST-MEMS.

Case 1

To start with, the bounds for speed and torque are taken from the raw data used for finding the fitting functions in Equation 3-3.

$$\begin{aligned}
\underline{\omega}_{ice} &= 83.76(\min(\omega)\text{from the raw data for ICE}) & \bar{\omega}_{ice} &= 251.31(\max(\omega)\text{from the raw data for ICE}) \\
\underline{\tau}_{ice} &= -86.15(\min(\tau)\text{from the raw data for ICE}) & \bar{\tau}_{ice} &= 689.84(\max(\tau)\text{from the raw data for ICE}) \\
\underline{\omega}_{mg1} &= 26.18(\min(\omega)\text{from the raw data for MG1}) & \bar{\omega}_{mg1} &= 811.57(\max(\omega)\text{from the raw data for MG1}) \\
\underline{\tau}_{mg1} &= -315(\min(\tau)\text{from the raw data for MG1}) & \bar{\tau}_{mg1} &= 315(\max(\tau)\text{from the raw data for MG1})
\end{aligned} \tag{4-1}$$

The power demand to the drive v_4 is given by a sinusoidal wave of amplitude 120 kW and frequency 1 rad/s as shown in Figure 4-1. The SOC is set as 50% and λ is set as 1. The other exogenous loads v_1, v_2, v_3 are set as 0.

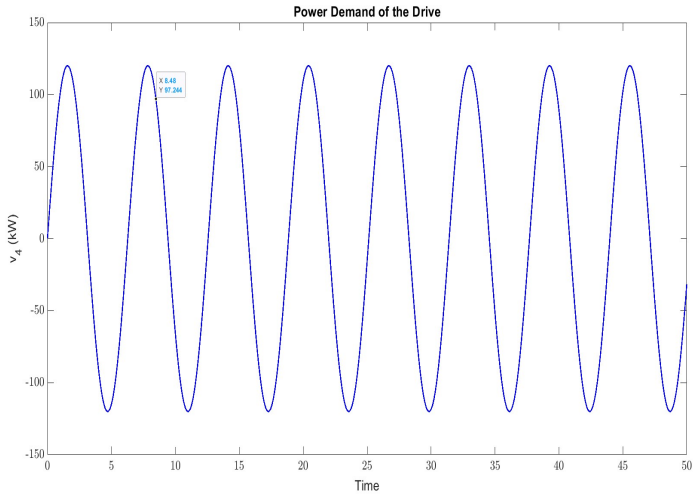

Figure 4-1: Power Demand of the Drive v_4

The speed of ICE in MEMS is chosen from a drive cycle to run MEMS.The ICE speed is plotted below and 180 rad/s is chosen as the value of the speed from this plot.

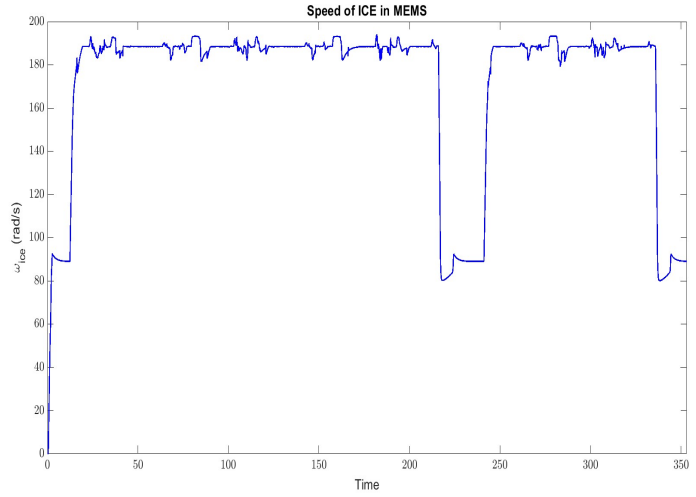

Figure 4-2: Speed of ICE - MEMS

First, the power loss function $\sum_{m\in\mathscr{M}}\sum_{k\in\mathscr{K}} c_m u_{m,k} - d_m y_{m,k}$ is calculated for both the MEMS and ST-MEMS and plotted together for comparison in Figure 4-3.

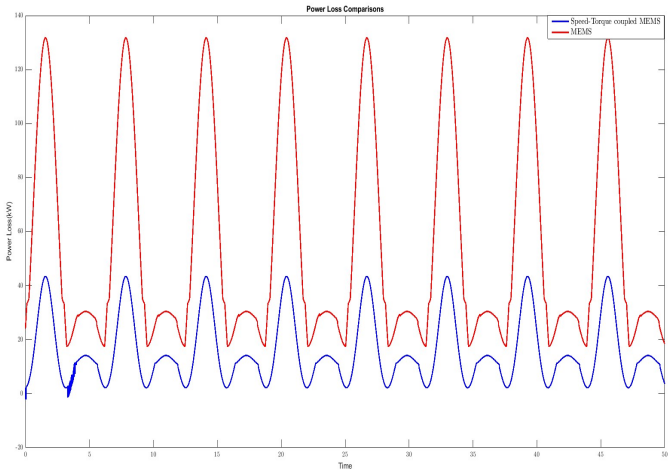

Figure 4-3: Power Loss Comparison - MEMS vs ST-MEMS (Case 1)

As shown above, the power loss is much lower for the ST-MEMS compared to the MEMS. To check if the constraints are satisfied, first the node balance in all 4 nodes is checked for both MEMS and ST-MEMS and plotted in Figure 4-4. From the plot, the power balance in the nodes is almost zero. It is also observed that the power balance in Node 1 reaches zero in the ST-MEMS case compared to the MEMS case.

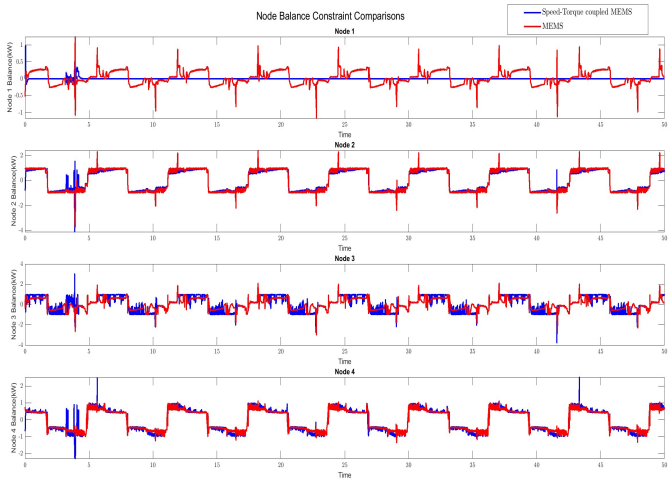

Figure 4-4: Total Power into and out of the Nodes (Case 1)

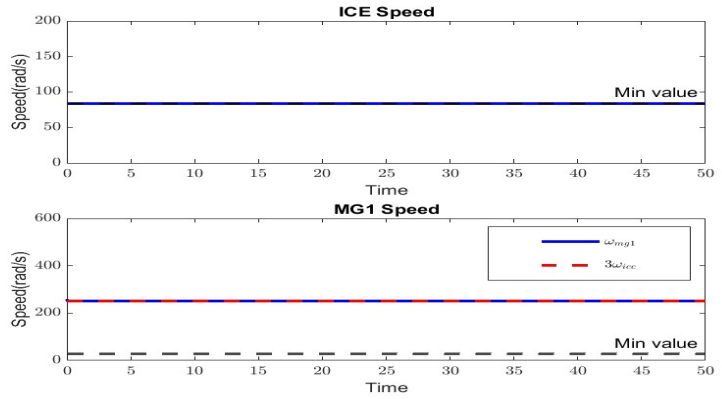

(a) Speed ω (Case 1)

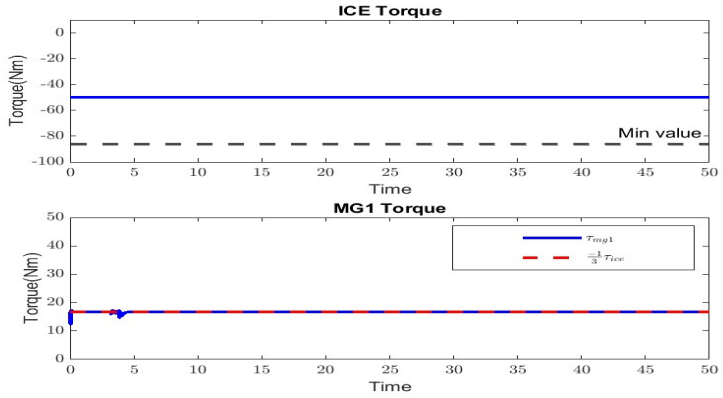

(b) Torque τ (Case 1)

Figure 4-5: Speed and Torque - ICE and MG1 (Case 1)

In case of the ST-MEMS, another constraint which needs to be satisfied is the gearset constraint coupling the speed and torque of ICE and MG1 given in Equation 3-9. Thus, the speed and torque for these 2 subsystems are plotted in Figure 4-5. Additionally, the minimum and maximum values for speed-and torque ($\underline{\omega}$, $\bar{\omega}$, $\underline{\tau}$, $\bar{\tau}$) are shown in the graphs.

The final check is with respect to the power demand, i.e., if y_{mg2} reaches v_4. This is checked in the plot in Figure 4-6. From the plots, it is observed that the power demand are satisfied.

From the speed-torque graph, it is observed that the ICE is run at minimum possible speed. For better comparison, output power from ICE and MG1 are also calculated and plotted for both MEMS and ST-MEMS case in 4-7b and 4-7c. From the plots, it is observed that the ICE-MG1 setup gives out lesser power in the ST-MEMS compared to MEMS which explains the lower power loss in ST-MEMS.

For Case 1, in ST-MEMS, the power demand is satisfied despite the ICE running in minimal possible speed, which means the HVB should provide higher power than the ICE and MG1 to satisfy the power requirements. This is checked by comparing the output power of the HVB of the speed-torque MEMS

to the same in MEMS in 4-7a.

It is observed that the output HVB power for the speed-torque MEMS is higher than the demanded power v_4 and the power output from ICE and MG1 are much lower in comparison. Thus, for this power demand, the algorithm chooses to use as much HVB power as possible to satisfy the demand. This result is kept as the base against which the inputs will be changed and compared to.

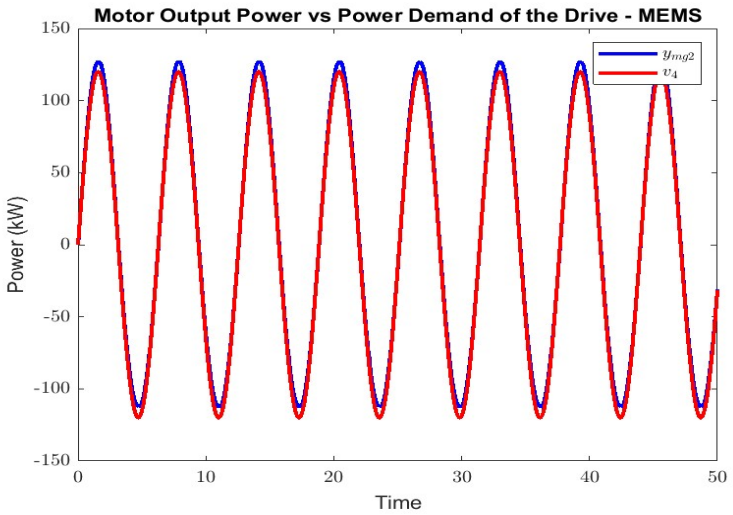

(a) MEMS (Case 1)

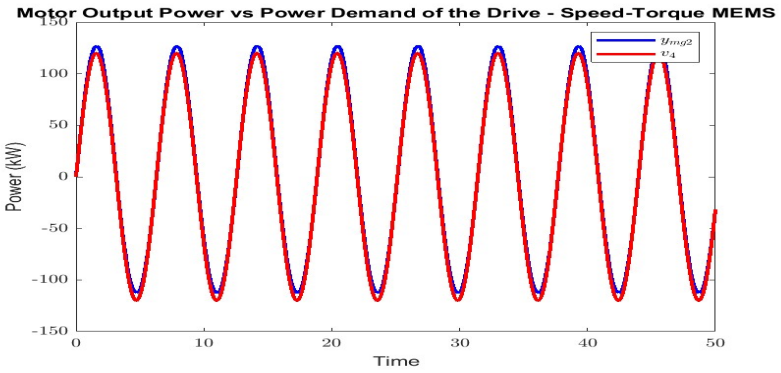

(b) ST-MEMS (Case 1)

Figure 4-6: Power Demand vs Motor Output Power (Case 1)

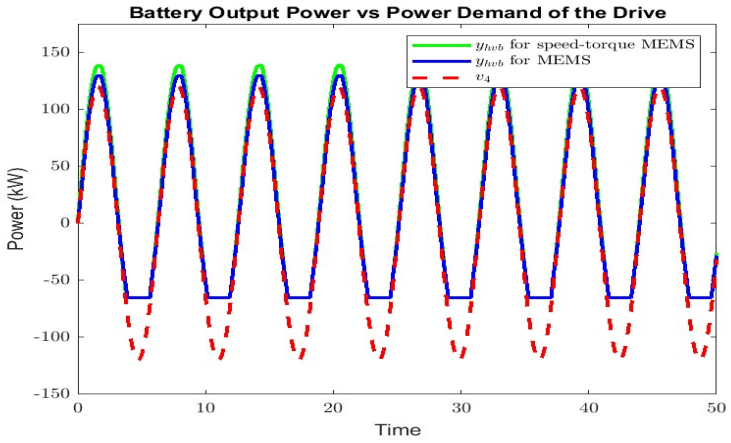

(a) Comparison of the output power of the HVB (Case 1)

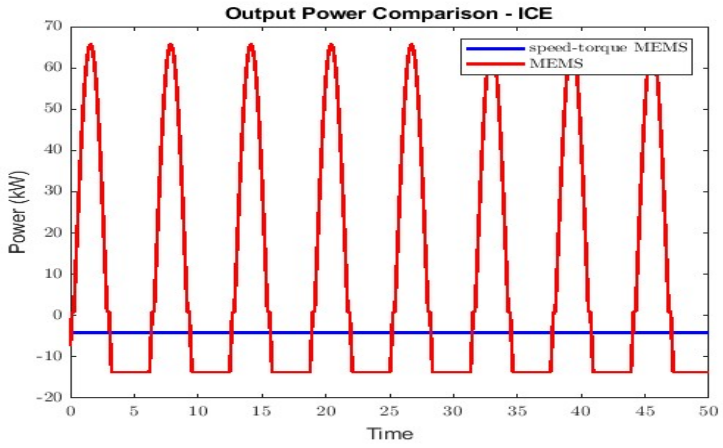

(b) Comparison of the output power of the ICE (Case 1)

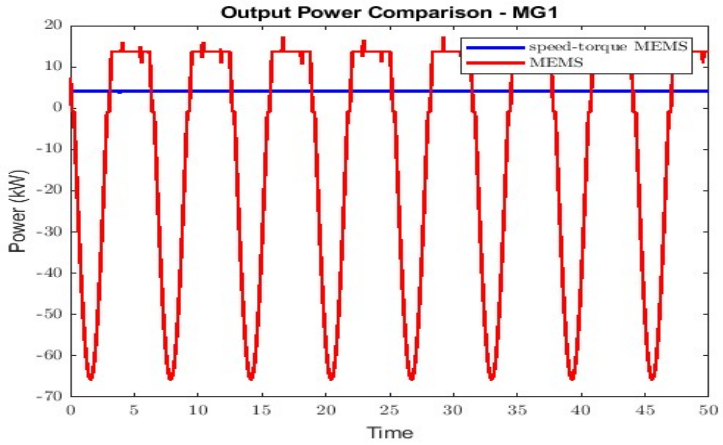

(c) Comparison of the output power of the MG1 (Case 1)

Figure 4-7: Subsystem Output Power Comparison (Case 1)

Case 2

To simulate this case, some of the inputs are kept the same as in Case 1. The changes applied are to the initial SOC which is now reduced to 10%. It is expected that more energy from the ICE will be used in comparison to the HVB as the HVB needs to be charged. In the Simulink block, it is programmed for the minimum charge to be 10%. Thus, consuming any more charge and taking it below 10% will make the algorithm infeasible.

Similar to the previous case, the power loss function is checked first by plotting the power loss as in Figure 4-8. Similar to the previous case, the power loss is much lower for the ST-MEMS.

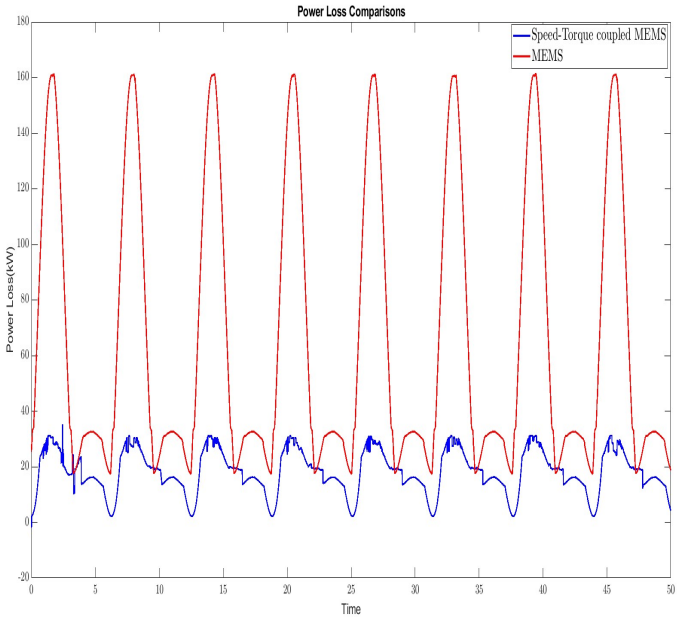

Figure 4-8: Power Loss Comparison - MEMS vs ST-MEMS (Case 2)

Now, the constraint checks are performed. First, the node balance constraints are checked. In this case, the MEMS satisfies the constraint better than ST-MEMS. There are some larger deviations from zero compared to the previous case. To understand the deviation, the output powers will be checked along with the speed-torque coupling constraint.

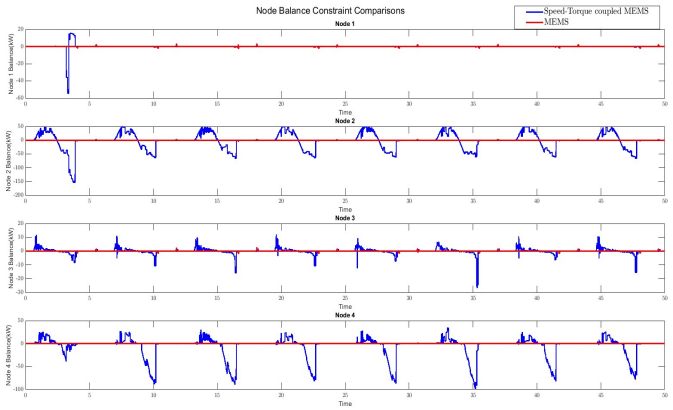

Figure 4-9: Total Power into and out of the Nodes (Case 2)

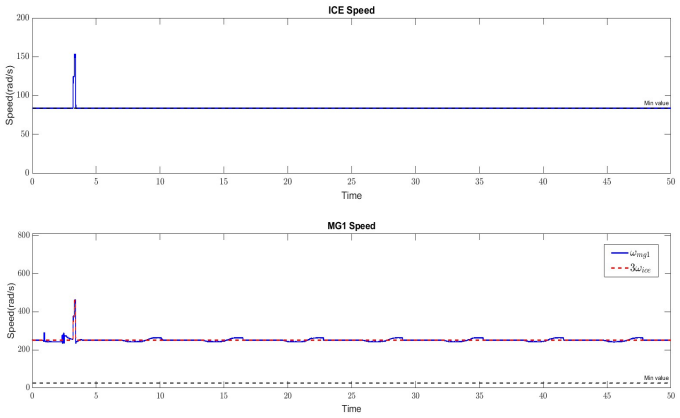

(a) Speed ω (Case 2)

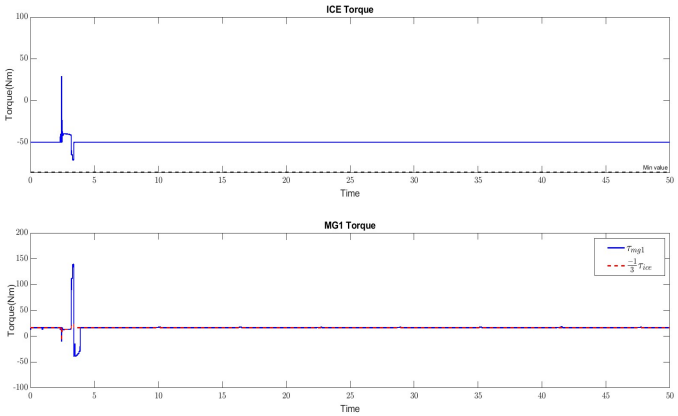

(b) Torque τ (Case 2)

Figure 4-10: Speed and Torque - ICE and MG1 (Case 2)

The gearset constraint coupling the speed and torque of ICE and MG1 is now checked. The speed and torque for these 2 subsystems, the minimum and maximum values for speed-and torque are plotted in Figure 4-10. From the plots, it is observed that there is an initial spike in the ICE speed and torque but then, it instantly reduces to the minimal speed again, thus operating the ICE only at the minimum required speed. However, the gearset constraint is satisfied.

The final check is if the power demand is satisfied as plotted in Figure 4-11. For MEMS, it is observed that the output power of the motor y_{mg2} is almost the same as in Case 1. However, there are slight deviations in the ST-MEMS which is causing the power imbalance at the nodes.

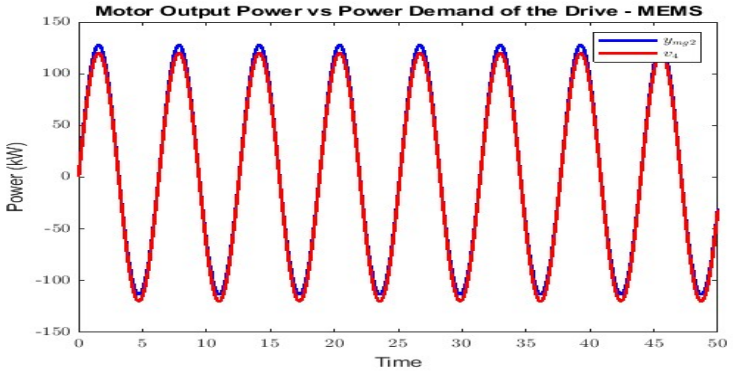

(a) MEMS (Case 2)

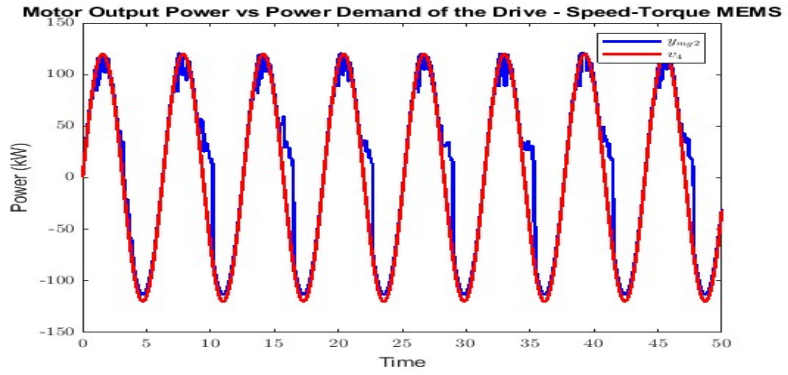

(b) ST-MEMS (Case 2)

Figure 4-11: Power Demand vs Motor Output Power (Case 2)

Similar to Case 1, it is important to compare the output power of the HVB of the ST-MEMS to the same in MEMS as seen in 4-12a. The HVB power is also compared to the output powers of ICE and MG1 which are plotted in 4-12b and 4-12c respectively.

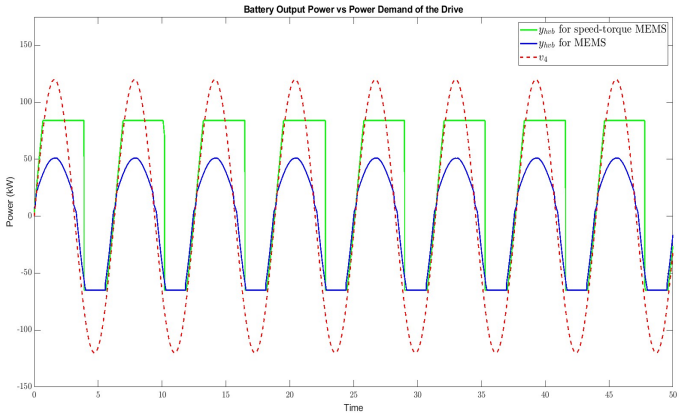

(a) Comparison of the output power of the HVB (Case 2)

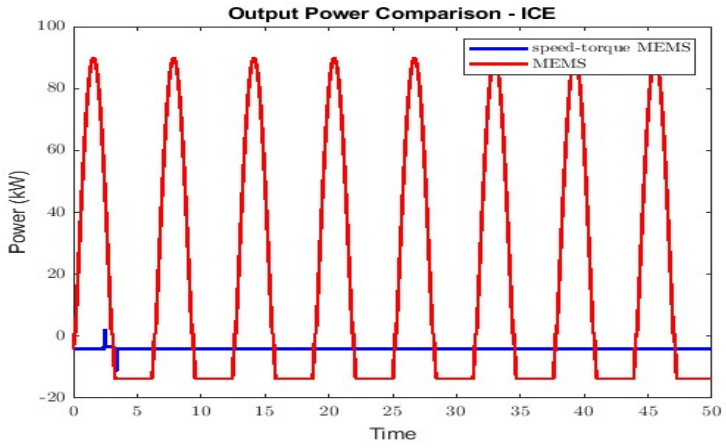

(b) Comparison of the output power of the ICE (Case 2)

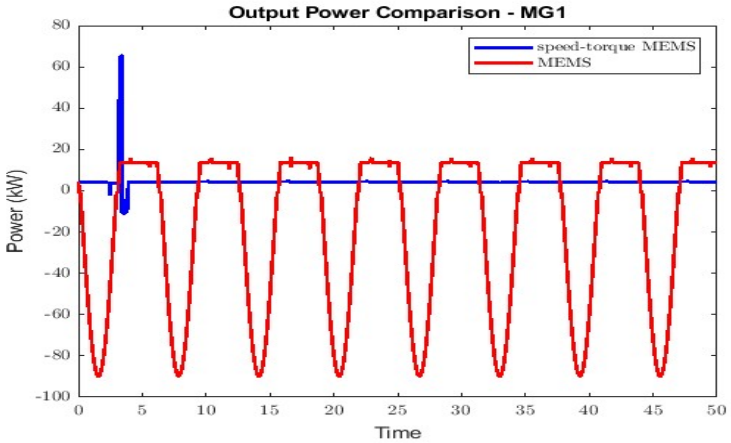

(c) Comparison of the output power of the MG1 (Case 2)

Figure 4-12: Subsystem Output Power Comparison (Case 2)

The output power for ICE and MG1 in case of ST-MEMS is similar except for the spike in the initial stages due to the spike in speed and torque. Thus, the output from the ICE-MG1 setup is still low. Comparing the output powers of the HVB to the case in 4-7a, the power is much lower in Case 2 as the HVB power is almost equal to the power demand in Case 1. Thus, Case 2 uses lesser HVB power as expected (due to the lower initial SOC).

Similarly, MEMS also uses much lesser power from the HVB in Case 2 compared to Case 1. Thus, the behaviour of MEMS and ST-MEMS is almost the same in terms of HVB usage. However, the power balance is not achieved in the latter.

It is important to investigate the reason for the nodal balance is investigated. The main difference from the previous case is the spike in speed. To analyze why the spike exists, the Lagrangian variables μ_1, μ_2, μ_3 are examined by plotting them as shown in Figure 4-13.

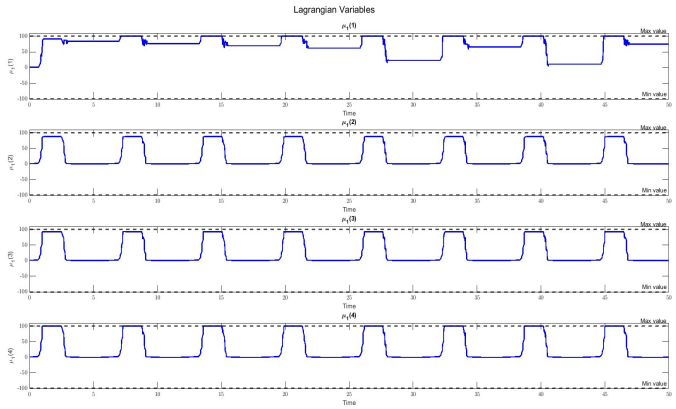

(a) μ_1 Individual Values (Case 2)

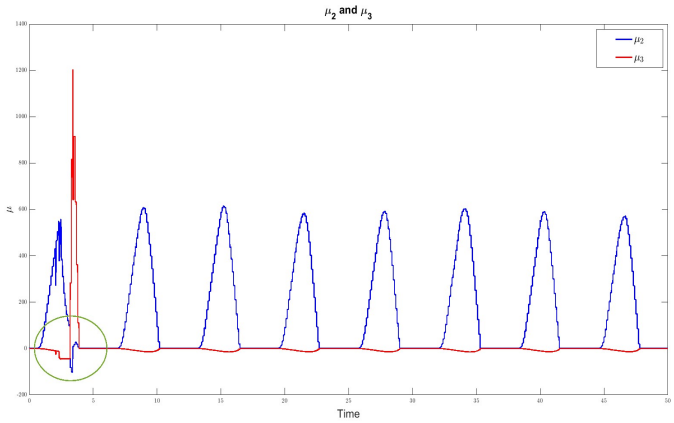

(b) μ_2 (Case 2)

Figure 4-13: Lagrangian Variables (Case 2)

While matching the time instance at which the spike in speed and torque occurs, the μ_2 and μ_3 values change instantly as indicated by the green circle in 4-14b. An attempt is made to saturate these Lagrangian variables. The bounds are tuned till the best possible result is obtained.

The bounds are $\mu_1 \in [-100, 100], \mu_2 \in [-1000, 1000], \mu_3 \in [-1000, 1000]$. The new Lagrangian variable update with these bounds is plotted in

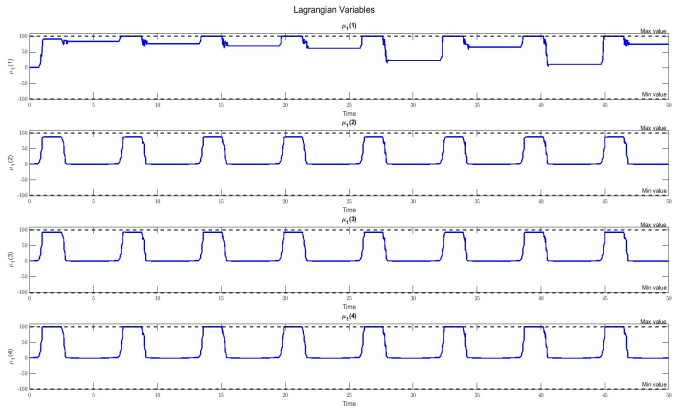

(a) μ_1 Individual Values (Case 2) with bounds

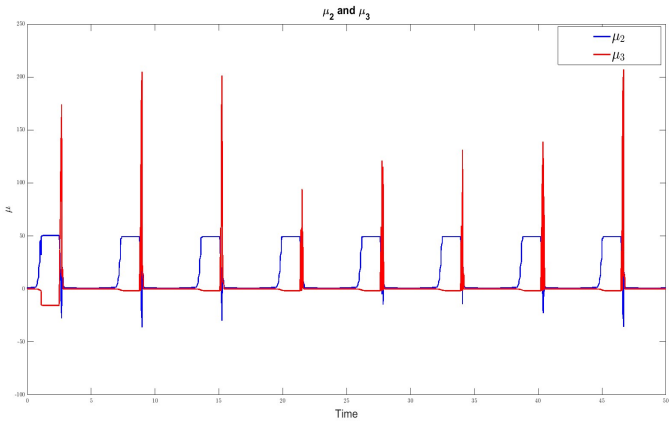

(b) μ_2 (Case 2) with bounds

Figure 4-14: Lagrangian Variables (Case 2) with bounds

The power balance in the nodes is checked first and plotted in Figure 4-15. As observed, the power balance improves in node 2. However, in node 4, there is a large power imbalance and in node 1, there are periodic spikes away from zero.

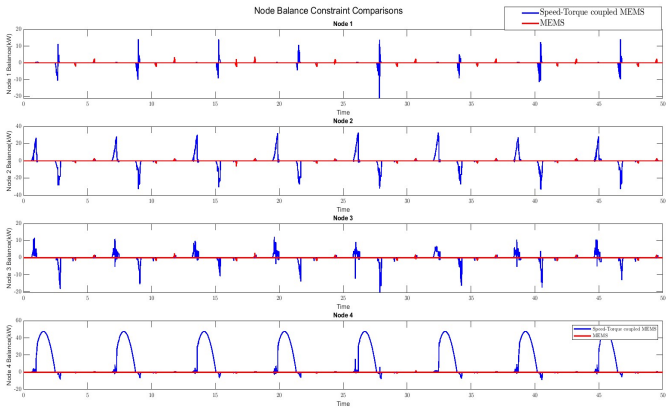

Figure 4-15: Total Power into and out of the Nodes (Case 2) with bounds on μ

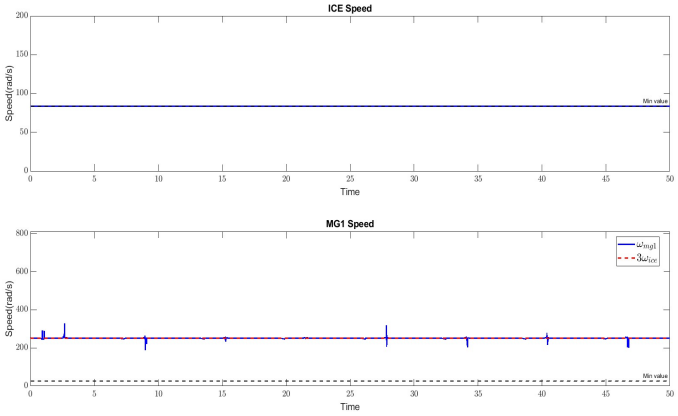

(a) Speed ω (Case 2) with bounds on μ

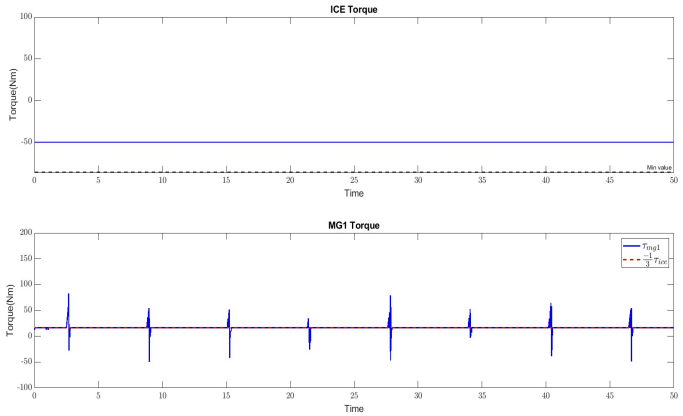

(b) Torque τ (Case 2) with bounds on μ

Figure 4-16: Speed and Torque - ICE and MG1 (Case 2) with bounds on μ

To check the imbalance in node 1, the speed and torque of ICE and MG1 are plotted and analyzed in Figure 4-16. The algorithm still runs the ICE in the lowest speed possible but there are few spikes in the torque. This causes the spikes in the power balance of nodes 1 and 2.

The reason for the imbalance in node 4 can be observed by plotting the Figure 4-17. There is clearly a deviation in the peak, i.e., the peak power is not achieved causing the imbalance in node 4.

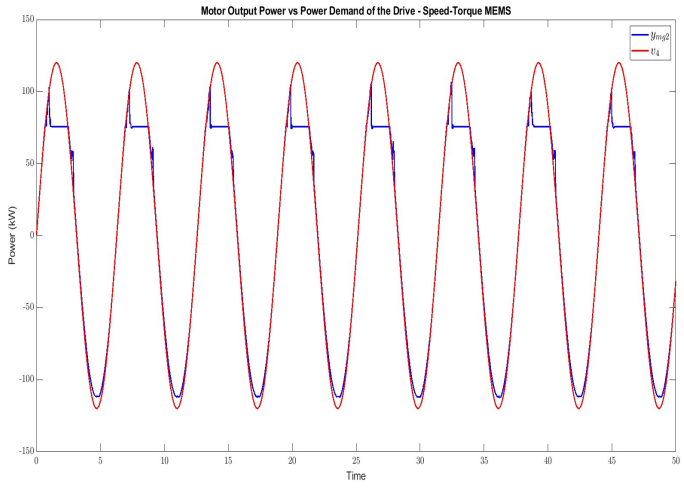

Figure 4-17: Power Demand vs Motor Output Power (Case 2) with bounds on μ

Thus, in this case, with the charge being low, the algorithm decides that the best possible scenario to achieve nodal power balance is to run the ICE at minimal power. The algorithm decides to not use the ICE despite not being able to use the HVB (as it is in low charge) and not achieving the full power demand.

Thus, in this case, there has to be a compromise between achieving better nodal power balance (with bounds on μ) and achieving power demand as close as possible (without bounds on μ). This is the first observed shortcoming of the algorithm, i.e., the ICE is not used properly even if forced to use it.

To confirm this hypothesis, the ICE is forced to operate at a much higher power (higher speed and torque) in the next case(s). The setup will be run at a different initial SOC and EF λ values to check if the ICE can operate appropriately in different HVB conditions according to the required power.

The checkpoints to verify the working of the OCP, i.e., the power loss, the power balance in the nodes and the speed-torque constraint are not reported. The main outputs to be examined and reported are the power out of ICE and HVB and how these results support the hypothesis.

Case 3

To force the ICE to operate at a higher power, the bounds of $\underline{\omega}_{ice}$, $\bar{\omega}_{ice}$, $\underline{\tau}_{ice}$, $\bar{\tau}_{ice}$ are increased. These bounds are set using the results of the previous cases from the original MEMS algorithm. They are set at -

$$\begin{aligned} \underline{\omega}_{ice} &= 180 \qquad \bar{\omega}_{ice} = 251.31 \\ \underline{\tau}_{ice} &= 444.44 \qquad \bar{\tau}_{ice} = 689.84 \\ \underline{\omega}_{mg1} &= 26.18 \qquad \bar{\omega}_{mg1} = 811.57 \\ \underline{\tau}_{mg1} &= -315 \qquad \bar{\tau}_{mg1} = 315 \end{aligned} \tag{4-2}$$

This case is divided into sub-cases :

3a) Initial SOC = 90%

3b) Initial SOC = 50%

3c) Initial SOC = 10%

The remaining inputs are kept the same as in Case 2. For Case 3b), the power loss function, constraints and power balance are not checked for the above cases.

First, the power loss function and constraints are checked for all cases. The plots are shown in Figure 4-18 - Figure 4-21 for Case 3b.

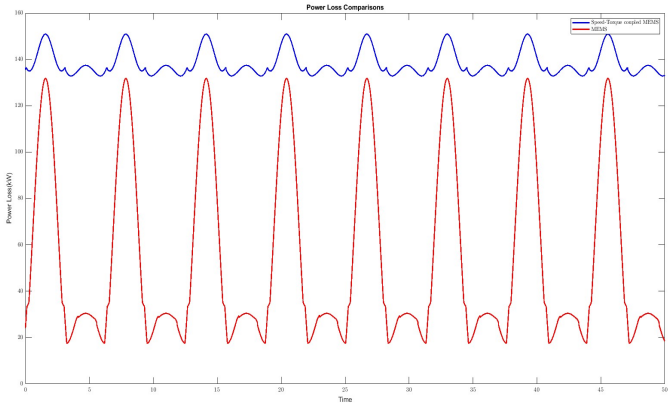

Figure 4-18: Power Loss Comparison - MEMS vs ST-MEMS (Case 3b)

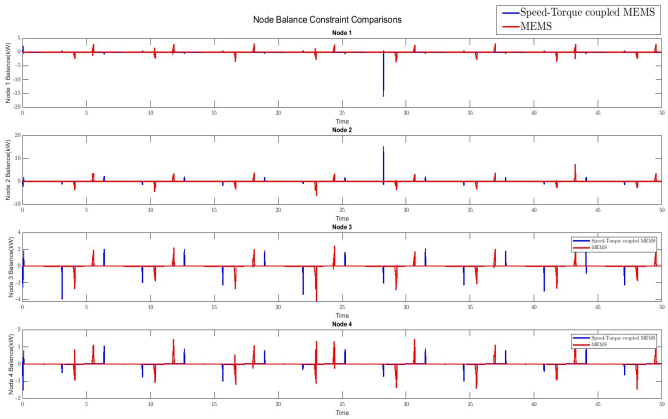

Figure 4-19: Total Power into and out of the Nodes (Case 3b)

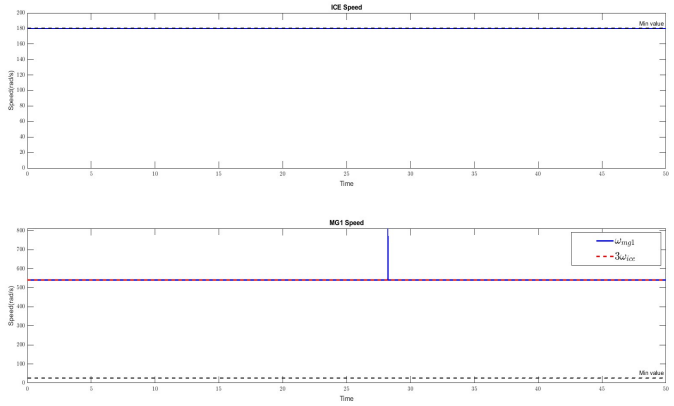

(a) Speed ω (Case 3b)

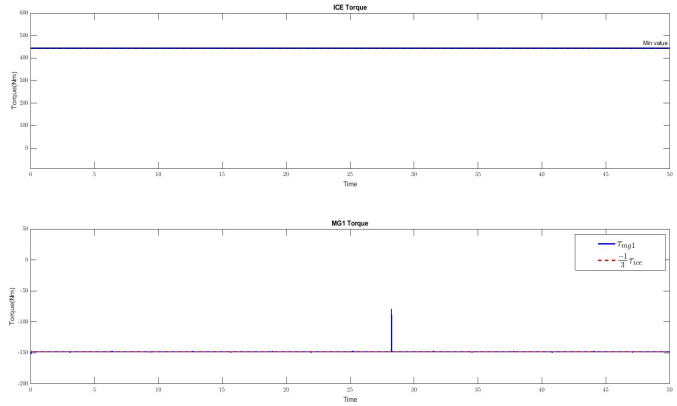

(b) Torque τ (Case 3b)

Figure 4-20: Speed and Torque - ICE and MG1 (Case 3b)

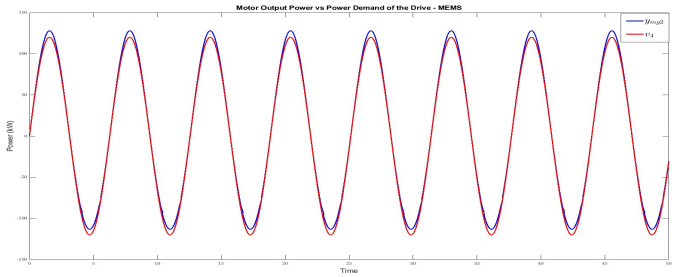

(a) MEMS (Case 3b)

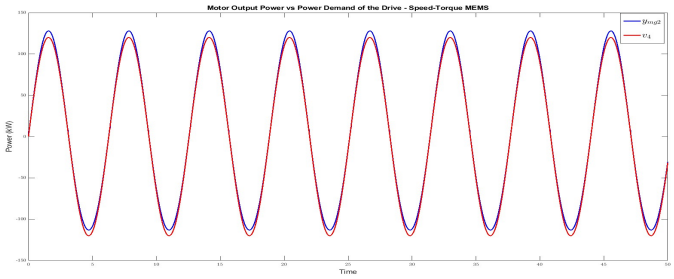

(b) ST-MEMS (Case 3b)

Figure 4-21: Power Demand vs Motor Output Power (Case 3b)

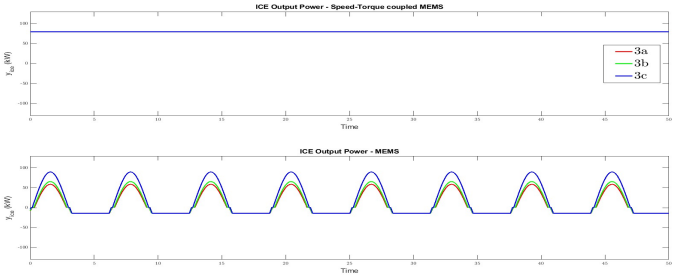

(a) Comparison of the output power of the ICE (Case 3b)

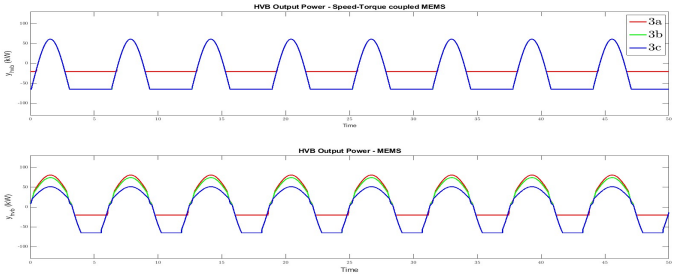

(b) Comparison of the output power of the HVB (Case 3b)

Figure 4-22: Subsystem Output Power Comparison (Case 3b)

The plots in Figure 4-18 - Figure 4-21 indicate that the power loss is lower in case MEMS and the constraints and power demand are satisfied in both MEMS and ST-MEMS. As discussed previously, the output powers of ICE and HVB are now compared for the 3 sub-cases with different initial SOCs by plotting them as seen in Figure 4-22.

From 4-22a, it is clear that the ST-MEMS produces the constant, minimum required power in the ICE, i.e. $y_{ice} = \underline{\omega}_{ice}\underline{\tau}_{ice}$. In comparison, MEMS, with increasing order of initial SOC, the output power of ICE decreases. This is consistent as a lower SOC forces the ICE to satisfy the power demand. This also explains why the power loss seen in Figure 4-18 is higher in ST-MEMS compared to MEMS. In ST-MEMS a constant minimum required power is produced irrespective of the power demand and in MEMS, the ICE output power follows a sinusoidal path to align with the instantaneous power demand. Thus, the power loss in ICE is higher in ST-MEMS. For a better comparison, the power loss in ICE alone ($u_{ice} - y_{ice}$) is plotted in Figure 4-23 and it is observed that the power loss is higher in ST-MEMS.

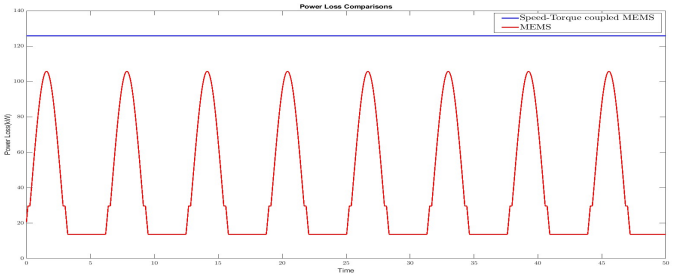

Figure 4-23: ICE Power Loss Comparison - MEMS vs ST-MEMS (Case 3b)

The HVB, on the other hand, produces a higher output power with a higher SOC as seen in 4-22b. In ST-MEMS, irrespective of the initial SOC, same amount of power comes out of the HVB. Even for initial SOC of 10%, the peak output power from the HVB is the same for ST-MEMS. However, in MEMS, the output power of the HVB increases with increasing initial SOCs. For both MEMS and ST-MEMS, the trough is lower in the negative axis compared to the other SOC cases. This is consistent as a lower negative value means higher power is given to the HVB to be charged.

The above obtained results support the hypothesis made after Case 2 about the ST-MEMS. On forcing the ICE to run by starting at a low HVB charge, the ICE still provides the minimum power possible and extracts the remaining required power from the HVB. In MEMS, the power distribution is managed between ICE and HVB in a better way by taking into account the initial SOC.

In the next case, the EF λ is be varied and the power distribution between the ICE and HVB is checked. Similar to Case 3, the power loss, the power balance in the nodes and the speed-torque constraint is reported only for one value of λ and the power out of ICE and HVB is checked for each value of λ.

Case 4

The bounds of $\underline{\omega}_{ice}$, $\bar{\omega}_{ice}$, $\underline{\tau}_{ice}$, $\bar{\tau}_{ice}$ are kept the same as in Case 3. The initial SOC is kept at 10%.

This case is also divided into sub-cases :

4a) $\lambda = 1$

4b) $\lambda = 5$

4c) $\lambda = 10$

The effect of increasing λ should be that higher priority is given to charge the HVB and use the ICE for satisfying the power demand.

Similar to the previous case, the power loss function is checked for one of the above cases, specifically, Case 4c.

First, the power loss function and constraints are checked for Case 4c. The plot is shown in Figure 4-24 for Case 4c.

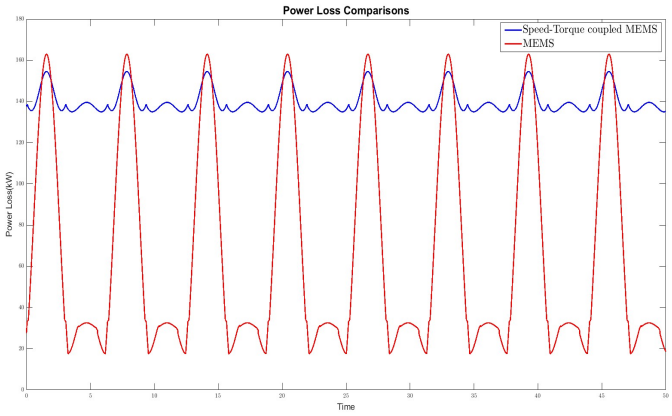

Figure 4-24: Power Loss Comparison - MEMS vs ST-MEMS (Case 4c)

Figure 4-24 indicates that the power loss for MEMS has a peak higher than ST-MEMS but overall, the former has a lesser power loss than the latter. The next step is to check the constraints and the power demand and they are satisfied as performed in Case 3b.

The output powers of ICE and HVB are now compared for the 3 sub-cases with different EF λ by plotting them as seen in Figure 4-25.

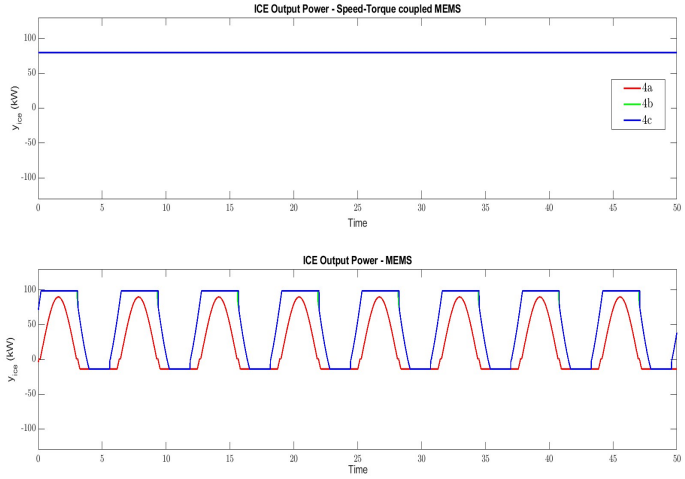

(a) Comparison of the output power of the ICE (Case 4)

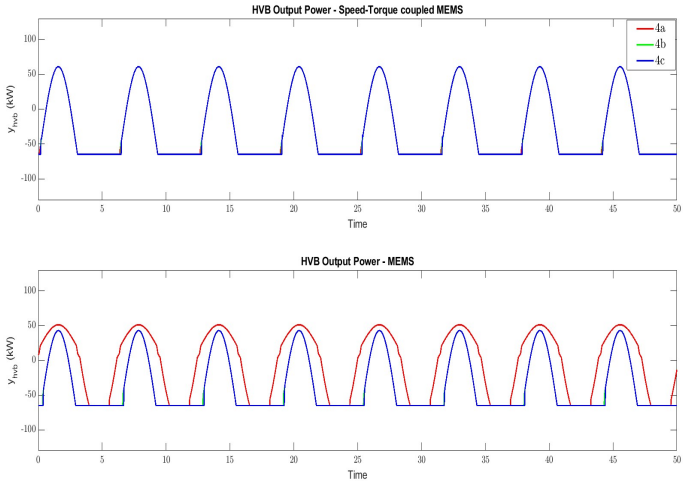

(b) Comparison of the output power of the HVB (Case 4)

Figure 4-25: Subsystem Output Power Comparison (Case 4)

While the the ST-MEMS produces the constant, minimum required power in the ICE as seen from 4-25a, MEMS produces higher output power in ICE for a higher λ. This is consistent as a higher λ forces the HVB to be charged and use the ICE to satisfy the power demand. As seen in Case 3b, the power loss in ICE alone ($u_{ice} - y_{ice}$) is plotted in Figure 4-26 to check if it explains the result in Figure 4-24. It is indeed observed that the power loss peak is higher in MEMS but in the remaining points, MEMS is able to achieve a lower power loss in comparison to ST-MEMS.

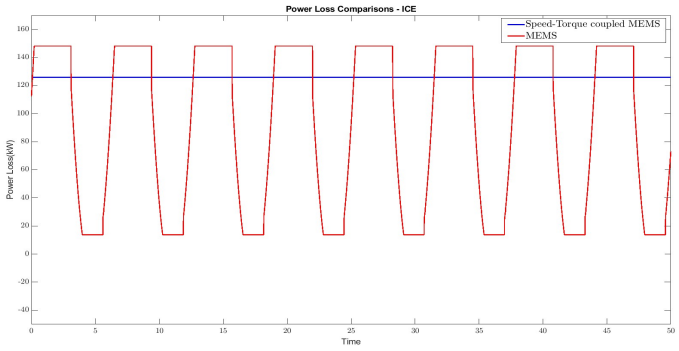

Figure 4-26: ICE Power Loss Comparison - MEMS vs ST-MEMS (Case 4)

The output power of HVB in 4-25b suggests that lower power is produced for higher λ values in MEMS, while the same amount of power is produced in ST-MEMS. Thus, irrespective of the λ value, the ST-MEMS produces the same power distribution while MEMS adjusts for λ.

The above obtained results support the hypothesis made after Case 2 about the ST-MEMS. On forcing the ICE to run by prioritizing HVB charging, the ICE still provides the minimum power possible and extracts the remaining required power from the HVB. In MEMS, the power distribution is managed between ICE and HVB in a better way by taking into account the EF λ.

Case 5

In this case, the effect of the minimum bounds of speed and torque of the ICE ($\underline{\omega}_{ice}$ and $\underline{\tau}_{ice}$). 3 cases are considered :

5a) $\underline{\omega}_{ice} = 180 \qquad \underline{\tau}_{ice} = 444.44$

5b) $\underline{\omega}_{ice} = 120 \qquad \underline{\tau}_{ice} = 300$

5c) $\underline{\omega}_{ice} = 100 \qquad \underline{\tau}_{ice} = 100$

The other bounds are kept the same as in the previous case. The initial SOC is set to 50% and λ is set to 1. For this case, the power loss function and the constraints are not focussed upon, but instead, the output power of the HVB and ICE is focussed upon.

In this case, only the MEMS is studied as the MEMS algorithm uses a constant known speed for ICE. The power distribution between ICE and HVB is examined for the different speed bounds. The output power of the ICE and HVB are plotted in Figure 4-27.

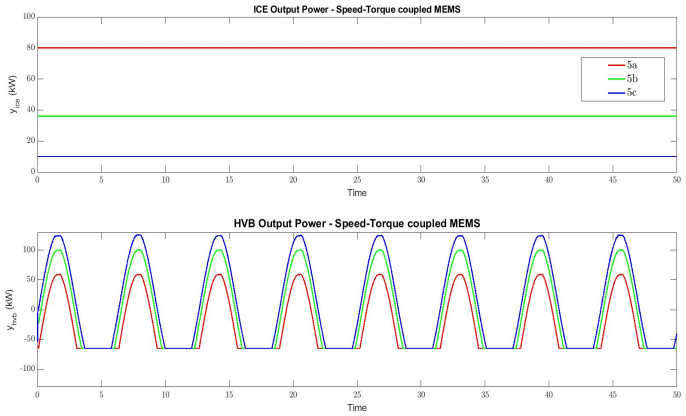

Figure 4-27: ICE Power Loss Comparison - MEMS vs ST-MEMS (Case 5)

From the plot above, the constant, minimum required power in the ICE, i.e. $y_{ice} = \underline{\omega}_{ice}\underline{\tau}_{ice}$ is produced for all bounds. Thus, the output power of the ICE is higher where the minimum required speed and torque are the higher. When the ICE gives higher power, the HVB power should give lesser power. It is observed that it is indeed the case, as the output power of the HVB is higher where the minimum required speed and torque are the lower. This result is ideal as it distributes the power between ICE and HVB properly.

Case 6

In all the previous cases, the ICE operated at the minimal speed an torque possible and the MG1 operated according to the gearset constraint. In this case, the ICE is forced to run at a higher speed and torque by increasing the minimum bounds of the MG1. The gearset constraint alone is checked in this case. The power loss function, node balance constraint and power demand is not checked.

The initial SOC is set as 50%, λ is set as 1 and other inputs are kept the same as in the previous case. The bounds are changed as :

$$\begin{aligned} \underline{\omega}_{ice} &= 100 \qquad \bar{\omega}_{ice} = 251.31 \\ \underline{\tau}_{ice} &= 200 \qquad \bar{\tau}_{ice} = 689.84 \\ \underline{\omega}_{mg1} &= 450 \qquad \bar{\omega}_{mg1} = 811.57 \\ \underline{\tau}_{mg1} &= -200 \qquad \bar{\tau}_{mg1} = -70 \end{aligned} \tag{4-3}$$

The ST-MEMS algorithm is run and the speed and torque outputs are plotted in Figure 4-28. It is observed that by limiting the bounds of MG1, the ICE adapts to the change and it no longer runs

at its minimum speed and torque. This proves that the optimization algorithm ensures the gearbox constraint is satisfied and the algorithm is able to adjust itself to satisfy the bounds. Another interesting observation is that the algorithm chooses to run the MG1 at the maximum torque, thus making the ICE run at the minimum torque possible, as they follow reverse signs as per Equation 3-9. This means that the ST-MEMS algorithm chooses to run the ICE at the minimum possible power to reduce the overall power loss.

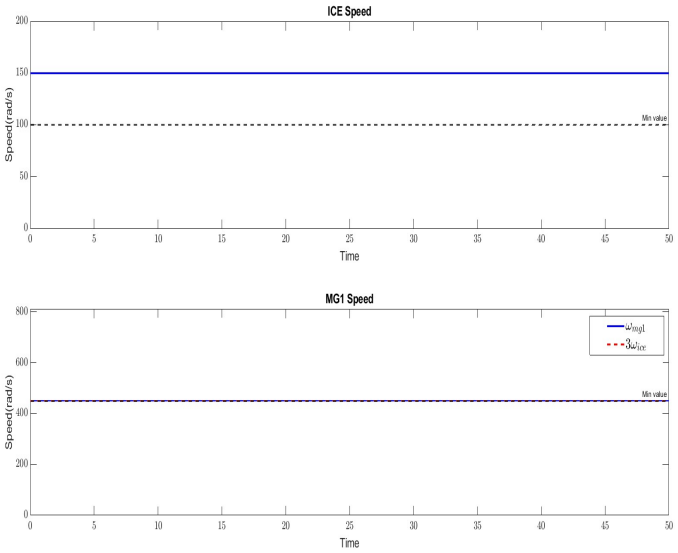

(a) Speed ω (Case 6)

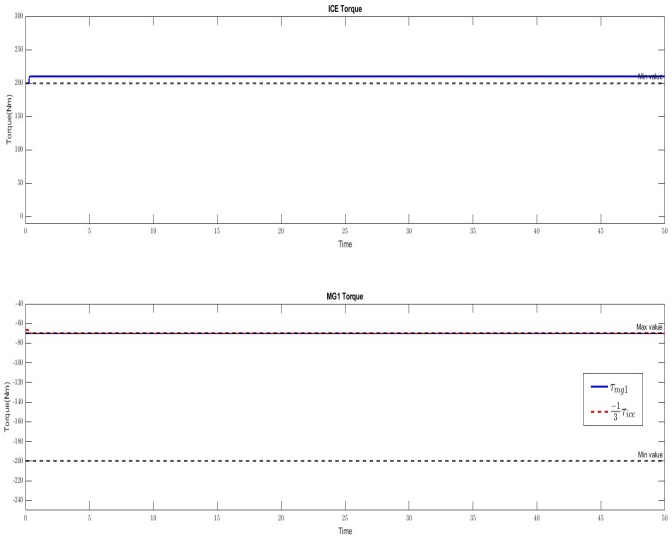

(b) Torque τ (Case 6)

Figure 4-28: Speed and Torque - ICE and MG1 (Case 3b)

Case 7

In this case, the effect of non-zero exogenous inputs are checked. Thus, v_1, v_2 is kept non-zero for this case, specifically :

$$\begin{aligned} v_1 &= 50 \text{ (affecting Node 1)} \\ v_2 &= 50 \text{ (affecting Node 2)} \end{aligned} \tag{4-4}$$

The rest of the inputs are kept the same as in the previous cases.

The power balance at the nodes are checked in this particular Casefor both MEMS and ST-MEMS as seen in Figure 4-29.

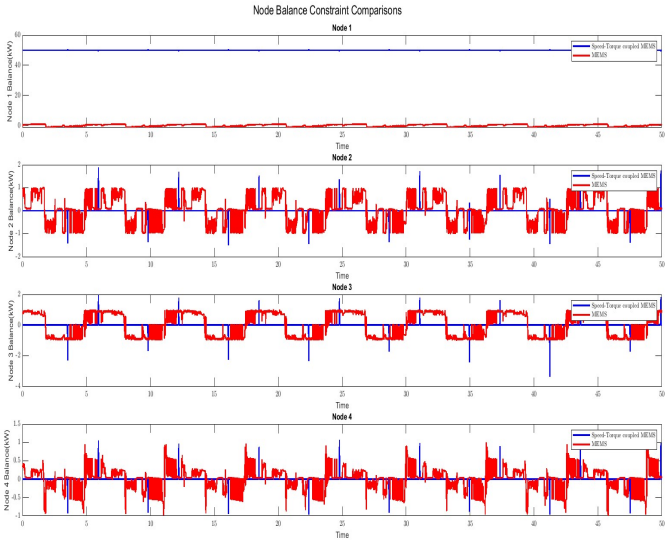

Figure 4-29: Total Power into and out of the Nodes (Case 7)

As observed, the power balance is not affected for Node 2 in ST-MEMS but the sum of powers in and out of Node 1 equals to input exogenous load v_1 and not zero. The reasoning for this can be derived from Equation 2-2 as follows :

$$\begin{aligned} & v_1 - y_{ice} - y_{mg1} = 0 \\ \text{Taking LHS} : \; & v_1 - y_{ice} - y_{mg1} \\ & \text{From Equation 3-13} \\ & = v_1 - \omega_{ice}\tau_{ice} - \omega_{mg1}\tau_{mg1} \end{aligned} \tag{4-5}$$

Recalling that

$$\begin{aligned} y_{ice} &= \omega_{ice}\tau_{ice} \\ y_{mg1} &= \omega_{mg1}\tau_{mg1} \\ 3\omega_{ice} &= \omega_{mg1} \\ \frac{-1}{3}\tau_{ice} &= \tau_{mg1} \end{aligned} \tag{4-6}$$

Thus, LHS now becomes :

$$\begin{aligned} &= v_1 - \omega_{ice}\tau_{ice} - (3\omega_{ice})(\frac{-1}{3}\tau_{ice}) \\ &= v_1 - \omega_{ice}\tau_{ice} + \omega_{ice}\tau_{ice} \\ &= v_1 \neq 0 \end{aligned} \tag{4-7}$$

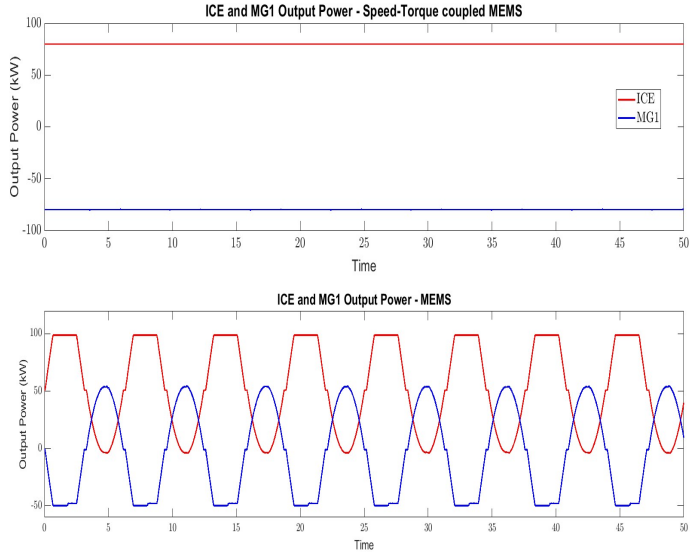

Figure 4-30: Comparison of the output power of the ICE and MG1 for MEMS and ST-MEMS(Case 7)

Thus, power balance can never be achieved in the nodes if the gearset constraints in Equation 3-9 are satisfied. Since ST-MEMS prioritizes this constraint, it ensures that $y_{ice} + y_{mg1} = 0$. However, in MEMS adjusts both the powers as per the load v_1. This is clear from the output power comparison plot in Figure 4-30. The output power of ICE and MG1 have the same magnitude but have opposite signs in ST-MEMS. However, in MEMS there is a difference in the peak of ICE and trough of MG1 thus showing that MEMS adjusts for satisfying the Node 1 constraint.

4-2 Advantages and Disadvantages of the ST-MEMS

From the results obtained in the Section 4-1, it is observed that the ST-MEMS has certain advantages in general and in comparison with MEMS. The advantages are :

- On introducing bounds for speed and torque, these constraints are satisfied in all cases. This makes the bounds for speed and torque for ICE and MG1 a degree of freedom, unlike MEMS where the bounds for power cannot be set and the speed of subsystems are not controllable.
- On operating MEMS and ST-MEMS in the speed and torque bounds given in the raw data, the power losses are significantly minimized in comparison with MEMS and the constraints are followed.
- Since most series-hybrid powertrains involve the same 2 subsystems (ICE and MG1), the modularity and flexibility is still preserved despite changing the optimization algorithm.

However, from the results, the below mentioned disadvantages are also observed :

- The ST-MEMS does not adapt well if the HVB cannot provide enough power. There are cases where the algorithm chooses to not satisfy the power demand when the HVB is limited in its operation. On the other hand, MEMS distributes the power between HVB and ICE according to the limitations of the HVB and ICE.
- On forcing the ICE to run on higher power and use lesser power from the HVB, i.e., the minimum bound chosen for the speed and torque is high, the power loss for ST-MEMS tends to be slightly higher than MEMS.
- In case of a non-zero exogenous load, ST-MEMS does not satisfy the power balance constraint in the nodes.

4-3 Alternate Suggestion

The disadvantages with ST-MEMS stem from the fact that the ICE runs at the minimal speed, torque and therefore minimum power possible. This limits the performance of the algorithm when the HVB is limited. This also leads to the imbalance of power in Node 1.

A possible reason is that the ICE and MG1 power is decided based on the speed and torque at which the power loss is minimum. The speed and torque are decided based on minimizing the power loss and this speed and torque is used to calculate the output power of these subsystems. Instead, the output power needs to be first decided for these subsystems and then the speed and torque needs to be fixed for that optimal output power such that the power loss is minimal.

The suggested algorithm is treated as a combination of MEMS and ST-MEMS and is formulated as follows. First the optimal power distribution is derived by solving the MEMS algorithm with the known data for subsystem speed in Equation 1-17.

$$u^*_{ice,k}, y^*_{ice,k}, u^*_{mg1,k}, y^*_{mg1,k} \ldots u^*_{bra,k}, y^*_{bra,k} = \arg \left(\begin{array}{l} \min\limits_{u_m, y_m} \sum\limits_{m \in \mathscr{M}} \sum\limits_{k \in \mathscr{K}} (c_m u_{m,k} - d_m y_{m,k} + \mu_k^T (\Gamma_m u_{m,k} + \Theta_m y_{m,k} + \frac{1}{M} v_k)) \\ \qquad + \lambda_k u_{hvb,k} \\ \text{s.t. } y_{m,k} + \frac{1}{2} q_{m,k} u^2_{m,k} + f_{m,k} u_{m,k} + e_{m,k} = 0 \\ \qquad \underline{u}_{m,k} \leq u_{m,k} \leq \bar{u}_{m,k} \end{array} \right) \tag{4-8}$$

From this optimal power distribution, the optimal speed (ω^*) and torque (τ^*) for ICE and MG1 is derived from Equation 3-16 as :

$$\begin{bmatrix} \omega^*_{m,k} \\ \tau^*_{m,k} \end{bmatrix} = \arg \left(\begin{array}{l} \min\limits_{\omega_{m,k}, \tau_{m,k}} \sum\limits_{k \in \mathscr{K}} \begin{bmatrix} \omega_{m,k} & \tau_{m,k} \end{bmatrix} Q_{m,k} \begin{bmatrix} \omega_{m,k} \\ \tau_{m,k} \end{bmatrix} + q_{m,k} \begin{bmatrix} \omega_{m,k} \\ \tau_{m,k} \end{bmatrix} \\ \text{s.t. } \omega_{m,k} \tau_{m,k} - y^*_{m,k} = 0 \\ \qquad \underline{\omega} \leq \omega_{m,k} \leq \bar{\omega} \\ \qquad \underline{\tau} \leq \tau_{m,k} \leq \bar{\tau} \end{array} \right) \tag{4-9}$$

The above method is implemented in MATLAB/Simulink and the working is analyzed in the below section by using the optimal power distribution results in MEMS. Thus, first the MEMS algorithm is implemented and outside this loop, the output power of the subsystems are given to another block to calculate the optimal speed and torque of the subsystems as per the optimal power distribution.

4-3-1 Results for Alternate Suggestion

For this section, a combination of multiple cases in section 4-1 is set as inputs. The main checkpoints will be if the constraints in Equation 4-9 are satisfied. The power balance in the nodes, the power demand and the output power distribution of the ICE and HVB with changing initial SOC and EF λ remain the same as in the results of MEMS in section 4-1. The reason for this is that the output power is derived from MEMS and the optimal power is then taken as a constant to solve the OCP to find the speed-torque distribution.

First the speed and torque is plotted as shown in Figure 4-31. It is observed that the gearset constraint is obeyed and the ICE is able to operate at a speed and torque above its preset minimal bounds. The speed and torque is also able to follow a sinusoidal path according to the power demand and output power as seen in the previous cases.

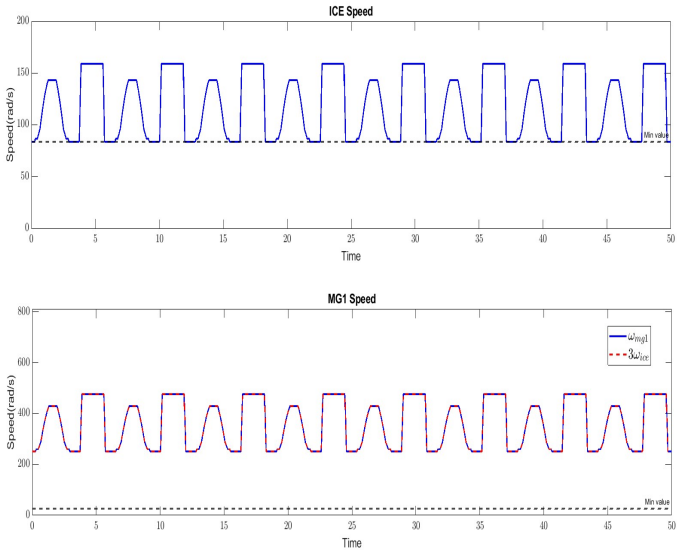

(a) Speed ω (Alternate Case)

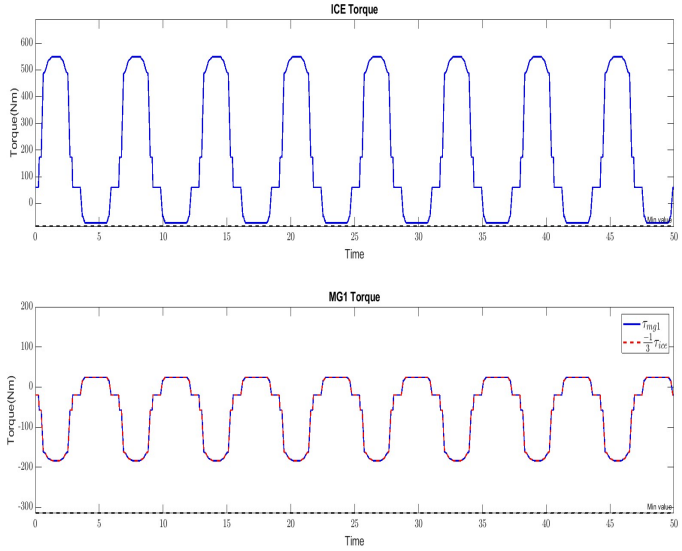

(b) Torque τ (Alternate Case)

Figure 4-31: Speed and Torque - ICE and MG1 (Alternate Case)

The next check is if the constraint in $\omega_{m,k}\tau_{m,k} - y^*_{m,k} = 0$ is obeyed as seen in Figure 4-32. It is observed that this condition is not fully satisfied. However, the speed-torque curves follow the trend of the output power curve and get saturated. This could be due to the non-convexity in the problem.

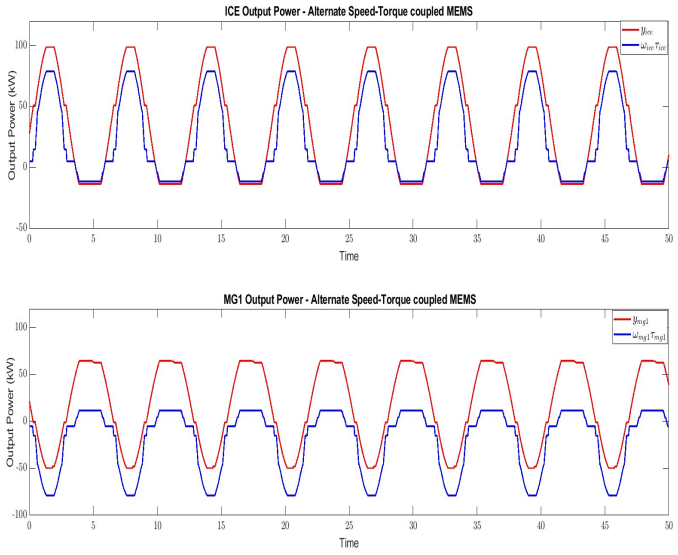

Figure 4-32: Output Power of ICE and MG1 vs Product of Speed and Torque- Alternate Case

The final check is if the speed and torque can be adjusted if the HVB is limited in its capacity. Thus, the speed and torque for ICE are plotted for $\lambda = 1$ and initial SOC at 10% and 50% in Figure 4-33. The speed of and torque of ICE at 10% is mariginally higher than those at 50%. The new algorithm clearly adjusts for a different initial SOC and extracts more from the ICE for a lower charge.

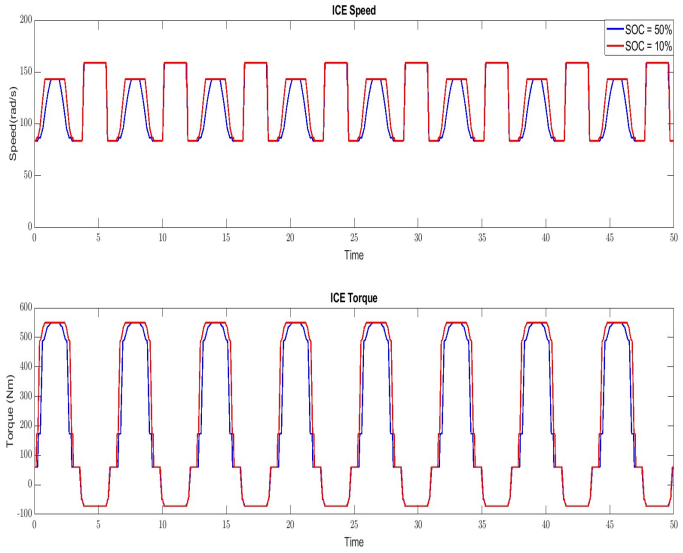

Figure 4-33: Speed and Torque for ICE for different SOC - Alternate Case

Next initial SOC is kept at 10% and λ is varied at 1 and 10 and the speed and torque are plotted in

Figure 4-34. The ICE runs at a lower speed and torque at the higher value of λ, which is consistent as the HVB needs to be charged and ICE needs to satisfy the power demand.The new algorithm clearly adjusts for a different EF and runs the ICE more for a higher EF.

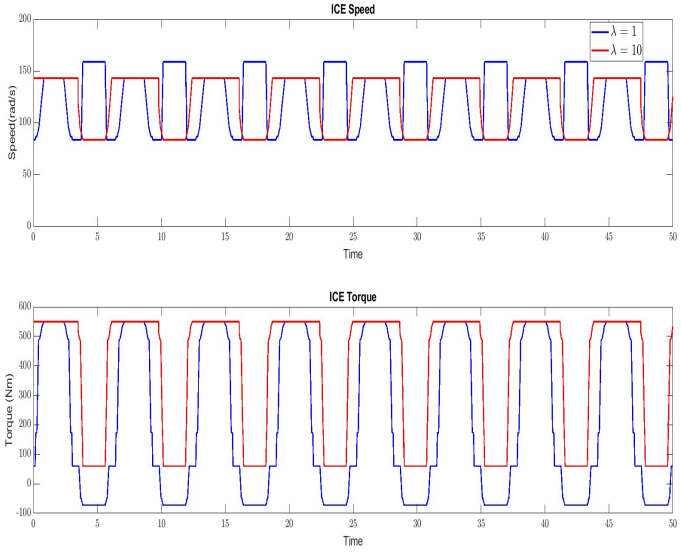

Figure 4-34: Speed and Torque for ICE for different λ - Alternate Case

Thus, the limitations that the ST-MEMS operates the ICE at minimal power despite the HVB being limited in its operation is solved here. The speed and torque is adjusted when the HVB is limited. Despite the theoretical limitations, this algorithm already proves that it is effective if the power distribution is decided first and then, the speed-torque distribution is decided. Also, the advantages of the ST-MEMS in terms of choosing the bounds for speed and torque for ICE and MG1 is preserved.

However, this method still uses the subsystem speed data to calculate the optimal power distribution. In an ideal situation, the power distribution has to be obtained without using the speed data to achieve the knowledge of optimal speed and torque. Additionally, the OCP in Equation 4-9 can be non-convex. Thus, the solution may not always be optimal.

4-4 Recommendations for Future Work

The factors which can be considered to improve the results of the work in this thesis are :

- A way to find the optimal power distribution without using the subsystem speed data such that this power distribution can be used to find the optimal speed and torque of operating the subsystems as per the obtained power distribution can be formulated. Additionally, methods can be explored to approximate the problem into a convex problem.

- The OCP can be extended to add other flow variables such as current to the MG2 apart from the subsystem speeds. Instead of the gearset, components like the DC/DC Converter and Inverter can be considered as nodes and power balance can be done in these nodes. It is possible to expand this notion to other systems like power grids, production lines, etc. which involve power flow and can be divided into nodes.
- The impact of hyper-parameters such as the Lagrangian variables μ_1, μ_2, μ_3 and their bounds can be explored.
- Implement the above methods in a closed-loop vehicle of a full vehicle and analyze other factors which impact the power distribution and how they can be optimized using methods such as A-ECMS which adjusts the hyper-parameter λ. Another factor which can be considered is increasing or decreasing the number of batteries connected in series/parallel which can impact the power from the ICE.
- Another aspect to be analyzed in the ST-MEMS is its performance with respect to computational time and iterations and comparison of these aspects with MEMS. As optimal power distribution is not achieved in the ST-MEMS implemented in this thesis, the analysis with respect to computational time is not performed.

Chapter 5

Conclusion

In this thesis, an HEV powertrain EMS called ECMS is introduced first. A modular algorithm called MEMS is introduced as an EMS and the formulation of its OCP is discussed. Its advantages with respect to how it derives the optimal power and torque distribution in the subsystems along with ensuring modularity, flexibility and computational speed is summarized. One of the shortcomings of the algorithm is that it does not consider powertrain subsystem speed an optimization variable and thus, the research question is raised : Can the subsystems be run at optimal speed along with power and torque ?

To achieve this, the objective functions and constraints in the OCP of MEMS are fitted as quadratic functions of speed and torque of the ICE and MG1. Least squares fitting is used for the quadratic function fittings. The MEMS OCP for ICE and MG1 is then converted to a quadratic programming problem of speed and torque of these subsystems as optimization variables. This new OCP is then termed as ST-MEMS used to find the optimal speed and torque.

The system used is the powertrain of a series-hybrid wheel loader and the powertrain topology is studied to formulate the ST-MEMS. The simulations for ST-MEMS is carried out in MATLAB/Simulink. A variety of cases with different inputs are simulated and their results are analyzed. The advantages observed are that the minimum and maximum bounds for speed and torque of the subsystems are added as degrees of freedom while preserving the optimality, modularity and flexibility of the original MEMS. the disadvantages, however, are that the ST-MEMS always runs the ICE at the minimum speed possible even if the HVB is limited and the power demand to the wheels of the vehicle is not satisfied, thus not providing an effective power distribution within the powertrain. A possible reason for this is that in ST-MEMS is that the speed and torque is first selected to minimize power losses. The suggestion is then given to first decide the optimal power distribution and then, the speed and torque

should then be decided to maintain this power distribution. To validate this, the MEMS algorithm is run to first find the optimal power distribution and then this result is used to find the optimal speed and torque distribution for the obtained optimal power such that the power loss is minimum for the obtained speed and torque as per the OCP in ST-MEMS. It is observed that using the power distribution to find the optimal speed and torque can combine the advantages of MEMS and ST-MEMS. However, this method cannot be considered sacrosanct as it still uses the speed information to obtain the optimal power distribution. Thus, for the future, it is important to derive a method to obtain an optimal power distribution without using the speed data to improve these results further.

Bibliography

[1] Netherlands Enterprise Agency. *Electric Vehicles Statistics in the Netherlands as of August 2022*. 2022. URL: https://www.rvo.nl/sites/default/files/2022-09/Statistics-elektric-vehicles-and-charging-in-the-Netherlands-up-to-and-including-August-2022.pdf.

[2] John Deere. *Doggett - Hybrid Wheel Loader - 944K*. URL: https://www.doggettequipment.com/equipment/construction/wheel-loader/hybrid-wheel-loader/hybrid-wheel-loader-944k.

[3] Shaojian Han, Fengqi Zhang, and Junqiang Xi. "A Real-Time Energy Management Strategy Based on Energy Prediction for Parallel Hybrid Electric Vehicles". In: *IEEE Access* 6 (2018), pp. 70313–70323. DOI: 10.1109/ACCESS.2018.2880751.

[4] Guoqiang Li and Daniel Görges. "Energy management strategy for parallel hybrid electric vehicles based on approximate dynamic programming and velocity forecast". In: *Journal of the Franklin Institute* 356.16 (2019), pp. 9502–9523. ISSN: 0016-0032. DOI: https://doi.org/10.1016/j.jfranklin.2019.09.011. URL: https://www.sciencedirect.com/science/article/pii/S001600321930643X.

[5] Yutong Li et al. "Research of regenerative braking system for electrified buses equipped with a brake resistor". In: *2013 IEEE Vehicle Power and Propulsion Conference (VPPC)*. IEEE. 2013, pp. 1–5.

[6] Qi Ma et al. "A high fidelity starter model for engine start simulations". In: *Proceedings of the 2005, American Control Conference, 2005.* 2005, 4423–4427 vol. 7. DOI: 10.1109/ACC.2005.1470692.

[7] T. Nilsson, A. Fröberg, and J. Åslund. "Predictive control of a diesel electric wheel loader powertrain". In: *Control Engineering Practice* 41 (2015), pp. 47–56. ISSN: 0967-0661. DOI: https://doi.org/10.1016/j.conengprac.2015.04.008. URL: https://www.sciencedirect.com/science/article/pii/S096706611500074X.

[8] Simona Onori, Lorenzo Serrao, and Giorgio Rizzoni. "Equivalent Consumption Minimization Strategy". In: *Hybrid Electric Vehicles: Energy Management Strategies*. London: Springer London, 2016, pp. 65–77. ISBN: 978-1-4471-6781-5. DOI: 10.1007/978-1-4471-6781-5_6. URL: https://doi.org/10.1007/978-1-4471-6781-5_6.

[9] Gino Paganelli et al. "General supervisory control policy for the energy optimization of charge-sustaining hybrid electric vehicles". In: *JSAE review* 22.4 (2001), pp. 511–518.

[10] J Park and J-H Park. "Development of equivalent fuel consumption minimization strategy for hybrid electric vehicles". In: *International Journal of Automotive Technology* 13.5 (2012), p. 835. DOI: https://doi.org/10.3390/en10081096.

[11] Constantijn Romijn et al. *Real-Time Distributed Economic Model Predictive Control for Complete Vehicle Energy Management*. 2017. DOI: 10.3390/en10081096. URL: https://www.mdpi.com/1996-1073/10/8/1096.

[12] T. Constantijn J. Romijn et al. "A Distributed Optimization Approach for Complete Vehicle Energy Management". In: *IEEE Transactions on Control Systems Technology* 27.3 (2019), pp. 964–980. DOI: 10.1109/TCST.2018.2789464.

[13] T.C.J. Romijn, T.H. Pham, and S. Wilkins. "Modular ECMS Framework for Hybrid Vehicles 11This work has received funding from European Union's Hori-zon2020 Programme for research and innovation under grant agreement No.724087." In: *IFAC-PapersOnLine* 52.5 (2019). 9th IFAC Symposium on Advances in Automotive Control AAC 2019, pp. 128–133. ISSN: 2405-8963. DOI: https://doi.org/10.1016/j.ifacol.2019.09.021. URL: https://www.sciencedirect.com/science/article/pii/S2405896319306408.

[14] Yassine Sabri, Najib El Kamoun, and Fatima Lakrami. "A Survey: Centralized, Decentralized, and Distributed Control Scheme in Smart Grid Systems". In: *2019 7th Mediterranean Congress of Telecommunications (CMT)*. 2019, pp. 1–11. DOI: 10.1109/CMT.2019.8931370.

[15] Lorenzo Serrao, Simona Onori, and Giorgio Rizzoni. "A Comparative Analysis of Energy Management Strategies for Hybrid Electric Vehicles". In: *Journal of Dynamic Systems, Measurement, and Control* 133.3 (Mar. 2011). 031012. ISSN: 0022-0434. DOI: 10.1115/1.4003267. eprint: https://asmedigitalcollection.asme.org/dynamicsystems/article-pdf/133/3/031012/5783955/031012_1.pdf. URL: https://doi.org/10.1115/1.4003267.

[16] Chao Sun, Hongwen He, and Fengchun Sun. “The Role of Velocity Forecasting in Adaptive-ECMS for Hybrid Electric Vehicles”. In: *Energy Procedia* 75 (2015). Clean, Efficient and Affordable Energy for a Sustainable Future: The 7th International Conference on Applied Energy (ICAE2015), pp. 1907–1912. ISSN: 1876-6102. DOI: https://doi.org/10.1016/j.egypro.2015.07.181. URL: https://www.sciencedirect.com/science/article/pii/S1876610215009492.

[17] Manh-Kien Tran et al. “Design of a Hybrid Electric Vehicle Powertrain for Performance Optimization Considering Various Powertrain Components and Configurations”. In: *Vehicles* 3.1 (2021), pp. 20–32. ISSN: 2624-8921. DOI: 10.3390/vehicles3010002. URL: https://www.mdpi.com/2624-8921/3/1/2.

Glossary

List of Acronyms

HEV	Hybrid Electric Vehicles
MEMS	Modular ECMS
EMS	Energy Management Systems
ECMS	Equivalent Consumption Minimization Strategy
DP	Dynamic Programming
ICE	Internal Combustion Engine
SOC	State-of-Charge
HVB	High Voltage Battery
BRA	Brakes
EM	Electric Machine
OCP	Optimal Control Problem
EF	equivalent factor
OB	Optimization-based
HVB	High-Voltage Battery
A-ECMS	Adaptive ECMS
MG	Motor/Generator
EBR	Electric Brake Resistor
GB	Gear Box
HP	Hydraulic Pump

BMS	Battery Management System
VAF	Variance Accounted For
ST-MEMS	Speed-Torque Coupled MEMS